



Numerical modelling and investigation of symmetric and asymmetric cavitation bubble dynamics

E. Lauer*, X.Y. Hu, S. Hickel, N.A. Adams

Lehrstuhl für Aerodynamik und Strömungsmechanik, Technische Universität München, Boltzmannstr. 15, 85748 Garching bei München, Germany

ARTICLE INFO

Article history:

Received 12 October 2011

Received in revised form 11 July 2012

Accepted 24 July 2012

Available online 3 September 2012

Keywords:

Bubble dynamics

Cavitation

Condensation/evaporation

ABSTRACT

In this paper, we investigate the high-speed dynamics of symmetric and asymmetric cavitation bubble-collapse. For this purpose, a sharp-interface numerical model is employed, that includes a numerically efficient evaporation/condensation model. The underlying assumption is that phase change occurs in thermal non-equilibrium and that the associated timescale is much larger than that of the wave-dynamics described by the interfacial Riemann problem. The sharp-interface model allows for an accurate tracking of the interface evolution throughout collapse and rebound. With a first set of simulations, we investigate the influence of the non-equilibrium on the relaxation behaviour of an oscillating vapour bubble. We observe that a good prediction of the phase-change rate is essential. Of high practical interest is the collapse of cavitation bubbles near walls under high ambient-pressure conditions. We investigate the differences in collapse evolution for detached and attached bubbles. It is shown that the maximum wall pressure strongly depends on the symmetry of the collapse mechanisms, and regions with a high probability of bubble rebound are identified. Asymmetric attached bubbles lead to significantly different topology changes during collapse than symmetric bubbles but exhibit roughly the same range of maximum pressures.

© 2012 Elsevier Ltd. All rights reserved.

1. Introduction

Cavitation is one of the major reasons for failure of technical devices involving the processing of liquids at large pressure differences. The collapse of cavitation bubbles causes erosion on marine propellers or water and steam turbines and on liquid-fuel injection nozzles. On the other hand, the destructive effects of cavitation can be exploited in medical application such as the shock wave lithotripsy.

Two fundamental phenomena are observed during the cavitation bubble collapse process. First Rayleigh [1] described the pressure increase upon bubble collapse; second Kornfeld and Suvorov [2] predicted the development of a re-entrant jet during non-spherical bubble collapse which occurs near solid walls. Both, the impact of shock waves and of the re-entrant jet on a surface can lead to strong material erosion. Progress in high-speed photography allowed for more detailed experimental investigations. Lindau and Lauterborn [3] visualised the propagation of shocks and the generation of the re-entrant jet for the bubble collapse close to a solid wall. Furthermore, they show the formation of a counter jet during the rebound, whose generating mechanism is still not fully understood. A more detailed experimental investigation is difficult

due to extremely small spatial and temporal scales, but numerical simulations provide a suitable tool for such flow configurations. The demands on the numerical methods are high, as wave dynamics strongly effect phase change and interface evolution.

In this paper, we use a model that is based on the conservative interface-interaction method of Hu et al. [4] The material interface is accurately resolved by a level-set approach on Cartesian meshes and the interface evolution is computed from a generalized Riemann problem.

Wave dynamics, such as shock wave propagation, determine the flow evolution in vapour and water throughout the final stages of collapse, whereas viscous effects and surface tension can be neglected throughout the relevant stages of a vapour bubble collapse [5]. Due to the violence of the bubble collapse, the comparatively slow process of heat diffusion is insignificant and leads to an approximately adiabatic system [6]. Thus, one set of Euler equations is formulated for each fluid (water and vapour) and discretized by a finite-volume scheme. Computational cells that are cut by the interface are subjected to a special treatment, where mass, momentum and energy exchanges at the interface are taken into account. The discretized equations are exactly conservative even for the interface interaction, unlike standard front-tracking methods. Topological changes at the interface are handled naturally by the employed level-set technique [7]. Interactions between both fluids at the interface are taken into account by approximate solutions of the generalized Riemann problem at the interface and by

* Corresponding author. Tel.: +49 89289 16143; fax: +49 89289 16139.

E-mail addresses: Eric.Lauer@aer.mw.tum.de (E. Lauer), Xianguy.Hu@tum.de (X.Y. Hu), sh@tum.de (S. Hickel), Nikolaus.Adams@tum.de (N.A. Adams).

introducing conservative exchange terms. While the original model of Hu et al. [4] deals only with momentum and energy exchange across the interface, the extended model which is used here includes the effect of phase-change phenomena such as evaporation and condensation.

The case of an oscillating gas or vapour bubble on one hand can be employed for the validation of a multi-phase model, on the other hand it allows to investigate the effect of a phase change model on the relaxation behaviour. Many authors e.g. [8–11] assess their interface models for the oscillating bubble, since conservation is essential for the results of this test case. Matula et al. [9] demonstrate experimentally and numerically, that the rate of phase change determines the bubble dynamics when the bubble contains vapour. The fact that according to Marek and Straub [12], the precise phase-change rate even for the extensively investigated combination of water and vapour is uncertain, demonstrates the need for further numerical and experimental investigation. The effect of the non-equilibrium assumption on the bubble oscillation in an acoustic field has been already investigated numerically e.g. [13–15]. The qualitative effect of the phase-change rate on the oscillation of a free spherical vapour bubble in water, presented in Section 5, is our first important result.

The main focus of our work is the asymmetric collapse of a cavitation bubble close to a solid wall under large liquid-pressure conditions. This problem has been studied extensively at atmospheric pressure level. Tomita and Shima [16] investigated the relationship between initial bubble stand-off distance and the maximum wall pressure, Vogel et al. [17] described the collapse mechanisms for a wide range of stand-off distances, Philipp and Lauterborn [18] focused on the resulting erosion at the boundary, Bremond et al. [19] studied the interaction of cavitation bubbles on a wall, and Gonzalez-Avila et al. [20] performed experiments in a liquid gap of variable height. Detailed wall pressure histories can be found in the work of Tong et al. [21]. While these authors presented results for detached as well as for attached cavitation bubbles, a precise determination of peak pressures at the wall and its association with the initial bubble configuration and evolution is beyond current experimental capabilities. Historically, investigations of cavitating flows have been motivated by cavitation erosion on ship propellers [22] and later especially by biomedical applications [23–25], where cavitation occurs at atmospheric ambient-pressure conditions. Therefore, the effect of large initial liquid pressure so far has not found much attention, although large ambient pressures occur in many technical applications, and thus are highly relevant in engineering. For example state-of-the-art high-pressure pumps for liquid-fuel injection operate at pressure levels up to 2500 bar [26], where cavitation is still likely to occur in high-velocity regions (throzzles, nozzles).

The first numerical results on the shape evolution of an initially spherical bubble during collapse near a solid wall have been obtained by Plesset and Chapman [27]. These results have been reproduced by many researchers with different multi-phase models. For example, Zhang et al. [28] used potential theory, Blake et al. [29] boundary integral methods, Popinet and Zaleski [30] free-surface boundary conditions and Sussman [31] a coupled level set and volume-of-fluid method for their calculations, assuming the liquid to be incompressible. Later, Iloreta et al. [24] studied the influence of the wall topology on cavitation. Johnsen and Colonius [5] investigated the vapour bubble collapse close to a solid wall taking into account the compressibility of the fluids and provided a study of the influence of the bubble stand-off distance to the wall onto the maximum wall pressure. Mueller et al. [32] described the emission of shock waves into the ambient liquid during bubble collapse using the method of Saurel and Abgrall [33]. Klaseboer et al. [34] investigated the effect of bubble collapse on an elastic infinite interface, Freund et al. [35] the effect on a viscous layer, and Shukla

et al. [36] the effect on a copper surface. Phase change was neglected in all these computations.

Shima and Nakajima [37] have considered non-spherical bubbles attached to a solid wall. Potential theory was used to investigate the different collapse mechanisms that arise for different initial bubble configurations. The collapse of a spherical bubble cut by a wall in its lower hemisphere was investigated with potential theory and compared with experimental data by Blake et al. [38] and Pearson et al. [39]. The effect of reflected shock waves on the collapse of attached and detached cavitation bubbles was described by Calvisi et al. [40]. These studies cover only the early stages of bubble collapse, since potential theory fails at later times when the bubble shape changes extremely fast. To the knowledge of the authors, there are no published numerical investigations on the collapse of wall-attached vapour bubbles using state-of-the-art numerical models that allow for an accurate simulation of the high-speed dynamics of the late stages of bubble collapse. The effect of high initial liquid pressures on the collapse mechanisms is unexplored.

Our simulation results take full account of compressibility and phase change. Different bubble wall configurations, attached and detached, symmetric and asymmetric, are investigated. Results in Section 6 provide insight into the different near-wall collapse mechanisms of spherical vapour bubbles and the time-evolution of wall pressure. The maximum wall pressure is considered as an indication of potential damage [41]. The effect of an initial bubble-shape variation is studied in Section 7 by considering the collapse of an ellipsoidal vapour bubble close to a solid surface. The objective of the present paper is to contribute to the clarification of wall-attached cavitation bubble collapse. In particular, we will demonstrate the importance of initial bubble shape on extreme events (maximum wall pressure, liquid jets) and the significance of initial bubble asymmetry on the collapse dynamics.

2. Governing equations

As convective effects dominate the cavitation bubble collapse, we neglect viscosity in the following computations. Viscosity may have a small quantitative effect, but does not affect the overall evolution. For a single fluid, we consider the three-dimensional Euler equations in conservative form:

$$\frac{\partial \mathbf{U}}{\partial t} + \frac{\partial \mathbf{F}_i(\mathbf{U})}{\partial x_i} = 0, \quad (1)$$

with the solution vector $\mathbf{U} = [\rho, \rho u_1, \rho u_2, \rho u_3, E]$. Density ρ , momentum $\rho \mathbf{u}$ and energy E (all volume specific) are the conserved variables, and \mathbf{u} is the velocity vector. The flux vectors are given by

$$\mathbf{F}_i(\mathbf{U}) = \begin{pmatrix} u_i \rho \\ u_i \rho u_1 + \delta_{i1} p \\ u_i \rho u_2 + \delta_{i2} p \\ u_i \rho u_3 + \delta_{i3} p \\ u_i (E + p) \end{pmatrix}. \quad (2)$$

2.1. Ideal gas

For an ideal gas, the pressure is determined from

$$E = \frac{1}{\gamma - 1} p + \frac{1}{2} \rho \mathbf{u}^2. \quad (3)$$

The ideal gas equation of state is

$$T = \frac{p}{R\rho}, \quad (4)$$

with the specific gas constant R . We model vapour as an ideal gas with $\gamma = 1.335$ and $R = 461.5 \text{ J/(kg K)}$.

2.2. Water-like fluids

For water-like fluids, we apply Tait's equation of state. The temperature T is assumed to be constant at 293 K, and pressure p and total energy E are functions of density ρ only

$$p = B \left(\frac{\rho}{\rho_0} \right)^\gamma - B + A, \quad (5)$$

$$E = \frac{1}{\gamma - 1} (p + B - A) + B - A + \frac{1}{2} \rho \mathbf{u}^2. \quad (6)$$

The parameters B , A and ρ_0 are constant. For liquid water, we set $B = 3310 \text{ bar}$, $A = 1 \text{ bar}$, $\rho_0 = 1 \text{ kg/m}^3$ and $\gamma = 7.15$ [7]. Since the total energy is only a function of density and velocity, the energy evolution is omitted from Eqs. (1) and (2).

3. Numerical method

For our simulations, we employ the conservative interface-interaction method proposed by Hu et al. [4] with an extension to three dimensions. The computational domain Ω is divided by the sharp interface $\Gamma(t)$ into two different subdomains $\Omega_1(t)$ and $\Omega_2(t)$. The volume $\Omega_1(t)$ accounts for the region occupied by fluid 1 and $\Omega_2(t)$ refers to the region occupied by fluid 2. We solve Eq. (1) for each fluid on the respective subdomain $\Omega_m(t)$ ($m = 1, 2$) on a three-dimensional Cartesian grid with spacings $\Delta x(i)$ $\Delta y(j)$ $\Delta z(k)$. Integrating Eq. (1) over the space–time volume $V \cap \Omega_m(t)$ of a computational cell (i, j, k) , the finite volume discretization follows:

$$\int_n^{n+1} dt \int_{V \cap \Omega_m(t)} dxdydz \left(\frac{\partial \mathbf{U}_m}{\partial t} + \nabla \cdot \mathbf{F}(\mathbf{U}_m) \right) = 0, \quad (7)$$

where \mathbf{U}_m is the vector of conservative variables for the considered fluid. The fluid volume $V \cap \Omega_m(t)$ can be expressed as $\alpha_m(t) \Delta x \Delta y \Delta z$, where $\alpha_m(t)$ is the time dependent fluid volume fraction of the considered cell and fluid m with $\alpha_1(t) + \alpha_2(t) = 1$. Applying the Gauss theorem one obtains

$$\int_n^{n+1} dt \int_{V \cap \Omega_m(t)} dxdydz \frac{\partial \mathbf{U}_m}{\partial t} + \int_n^{n+1} dt \int_{\partial(V \cap \Omega_m(t))} dxdydz \mathbf{F}(\mathbf{U}_m) \cdot \mathbf{n} = 0, \quad (8)$$

where $\int_{V \cap \Omega_m(t)} dxdydz$ is the volume integral over the domain covered by the corresponding fluid, and $\int_{\partial(V \cap \Omega_m(t))} dxdydz$ is the area integral over the cell faces $\partial(V \cap \Omega_m(t))$.

Defining the interface as $\Gamma(t) = V \cap \partial \Omega_m(t)$, the term $\partial(V \cap \Omega_m(t))$ can be expressed as the combination of two elements. The first element is the sum of the cell surfaces obtained by intersecting the interface with the cell faces, which can be expressed as $A_m^{11} \Delta y \Delta z$, $A_m^{12} \Delta y \Delta z$, $A_m^{21} \Delta x \Delta z$, $A_m^{22} \Delta x \Delta z$, $A_m^{31} \Delta x \Delta y$, $A_m^{32} \Delta x \Delta y$, where A_m^{pq} represents the so called cell-face aperture described in Fig. 1 and with $A_1^{pq} + A_2^{pq} = 1$. The second element $\Delta \Gamma(t)$ represents the surface of the portion of the interface within the cell (i, j, k) .

$$\bar{\mathbf{U}} = \frac{1}{\alpha_m(t)V} \int_{\alpha_m(t)V} \mathbf{U} dxdydz. \quad (9)$$

Eq. (8) can be rewritten in the following form:

$$\begin{aligned} & V(\alpha_m^{n+1} \bar{\mathbf{U}}_m^{n+1} - \alpha_m^n \bar{\mathbf{U}}_m^n) \\ &= \int_n^{n+1} dt \Delta y \Delta z \left[A_m^{12}(t) \mathbf{F}_m^{12} - A_m^{11}(t) \mathbf{F}_m^{11} \right] \\ &+ \int_n^{n+1} dt \Delta x \Delta z \left[A_m^{22}(t) \mathbf{F}_m^{22} - A_m^{21}(t) \mathbf{F}_m^{21} \right] \\ &+ \int_n^{n+1} dt \Delta x \Delta y \left[A_m^{32}(t) \mathbf{F}_m^{32} - A_m^{31}(t) \mathbf{F}_m^{31} \right] + \int_n^{n+1} dt \mathbf{X}_m(\Delta \Gamma(t)), \quad (10) \end{aligned}$$

where $\alpha_m \bar{\mathbf{U}}_m$ and $\bar{\mathbf{U}}_m$ are the vector of the conserved quantities in the cut cell and the vector of volume averaged conservative variables respectively. \mathbf{F}_m^{pq} is the average flux across a cell face and \mathbf{X}_m is the average mass, momentum and energy exchange across the interface.

Cell-face apertures, volume fractions and interface area are determined from a level-set field Φ , which describes the signed distance of any point from the immersed interface. The zero-level-set contour ($\Phi = 0$) represents the interface between the two fluids. This approach allows for the treatment of arbitrary geometries and can deal with moving and strongly deforming interfaces. The level-set field is updated following [7] and we employ the marching-square approach [42] to determine the face apertures. Assuming a linear approximation of the interface within a cell, the interface area $\Delta \Gamma$ is given by

$$\Delta \Gamma = \sqrt{\left((A_m^{12} - A_m^{11}) \Delta y \Delta z \right)^2 + \left((A_m^{22} - A_m^{21}) \Delta x \Delta z \right)^2 + \left((A_m^{32} - A_m^{31}) \Delta x \Delta y \right)^2}. \quad (11)$$

Geometrical reconstruction with seven pyramids leads to the volume fraction

$$\begin{aligned} \alpha_m = \frac{1}{\Delta x \Delta y \Delta z} & \left[\frac{1}{3} A_m^{11} \Delta y \Delta z \frac{\Delta x}{2} + \frac{1}{3} A_m^{12} \Delta y \Delta z \frac{\Delta x}{2} + \frac{1}{3} A_m^{21} \Delta x \Delta z \frac{\Delta y}{2} \right. \\ & \left. + \frac{1}{3} A_m^{22} \Delta x \Delta z \frac{\Delta y}{2} + \frac{1}{3} A_m^{31} \Delta x \Delta y \frac{\Delta z}{2} + \frac{1}{3} A_m^{32} \Delta x \Delta y \frac{\Delta z}{2} + \frac{1}{3} \Delta \Gamma \Phi_c \right] \quad (12) \end{aligned}$$

where Φ_c is the level-set value in the cell centre, representing the distance from the cell centre to the interface.

For full cells which are not cut by the interface, volume fractions and cell face apertures are unity, the corresponding interface surface fraction vanishes, and Eq. (10) simplifies to

$$\begin{aligned} V(\bar{\mathbf{U}}_m^{n+1} - \bar{\mathbf{U}}_m^n) &= \int_n^{n+1} dt \Delta y \Delta z \left[\mathbf{F}_m^{12} - \mathbf{F}_m^{11} \right] \\ &+ \int_n^{n+1} dt \Delta x \Delta z \left[\mathbf{F}_m^{22} - \mathbf{F}_m^{21} \right] \\ &+ \int_n^{n+1} dt \Delta x \Delta y \left[\mathbf{F}_m^{32} - \mathbf{F}_m^{31} \right], \quad (13) \end{aligned}$$

recovering a standard finite volume scheme on a three-dimensional Cartesian grid. Being effective only in the cells that are cut by the interface, this immersed interface method can be seen as a local modification of the standard finite volume scheme close to the interface.

In order to allow for using unmodified interpolation stencils for reconstruction close to the interface, we have to define fluid states for fluid 1 in the fluid 2 regime close to the interface and vice versa. For both fluids the volume averaged variables are extended to the opposite side of the interface by

$$\frac{\partial \bar{\mathbf{U}}_m}{\partial t_f} - \mathbf{n} \cdot \nabla \bar{\mathbf{U}}_m = 0, \quad (14)$$

where t_f is a pseudo time [4].

We use a fifth-order WENO scheme [43] and a third-order TVD Runge–Kutta scheme [44] to discretize the Euler equations. Computations are carried out with the CFL number of 0.6. In this paper, we always consider two-fluid problems containing vapour and water, i.e. effects due to dissolved gas are not considered. We always model vapour as ideal gas and use Tait's equation of state for water. Material properties are given in the corresponding material law section.

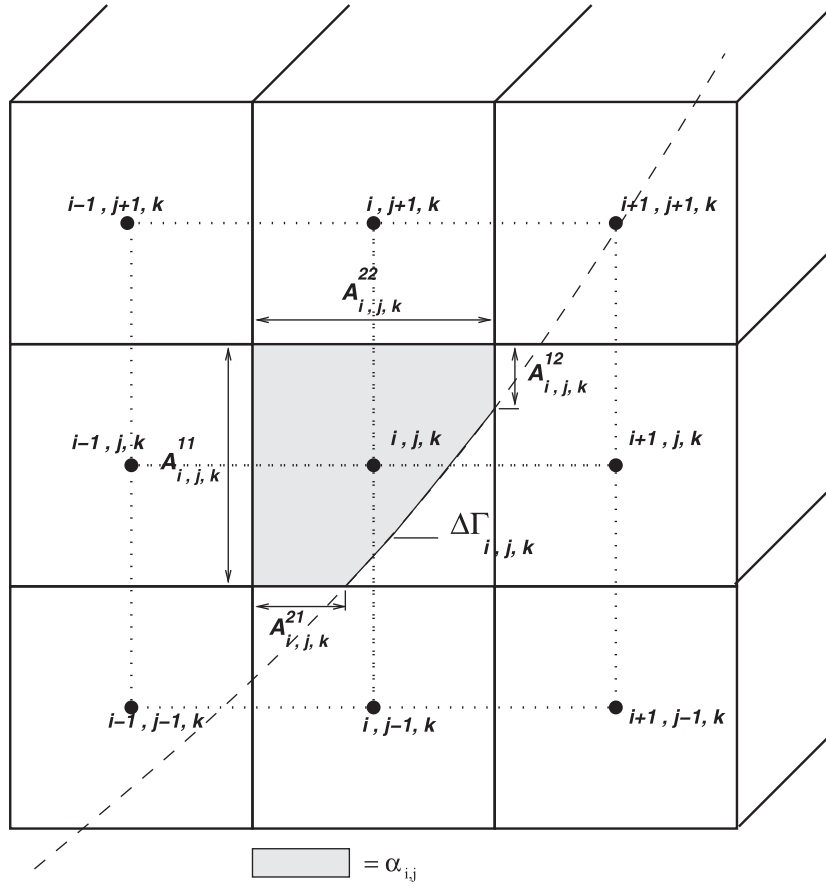


Fig. 1. Two-dimensional schematic of conservative discretization for a cut cell.

3.1. Interface interaction

Since the model of Hu et al. [4] does not account for mass transfer across the interface, we incorporate mass transfer into the interaction term $\mathbf{X}_m(\Delta\Gamma)$. Two separate terms describe the contributions of pressure force and phase change to the interface interaction, respectively,

$$\mathbf{X}_m(\Delta\Gamma) = \mathbf{X}_m^p + \mathbf{X}_m^f. \quad (15)$$

For viscous interactions, interface friction can be taken into account in a straight-forward way by introducing a no-slip correction at the interface. For large temperature differences between both fluids or for an evolution on large timescales, an additional heat transfer term can be formulated similarly. As mentioned above, here we suppress effects of heat flux and surface tension at the interface to comply with the observations of Johnsen and Colonius [5], Szeri et al. [6], and Popinet and Zaleski [30]. For collapsing bubbles close to wall, Popinet and Zaleski found an effect of viscosity on the collapse mechanisms for Reynolds numbers in the range of 10–100. Following their definition of the Reynolds number, we have $Re = Re_{equ} \sqrt{\rho_{li} p_{li}} / \mu_{li} \approx 5000$ for our set-up in Section 6, where Re_{equ} is the equilibrium bubble radius and μ_{li} is the viscosity of liquid water, respectively. This is two orders of magnitude larger than the critical value, and thus we neglect viscosity in our computations. A more detailed discussion on the potential effect of viscosity and surface tension at atmospheric conditions can be found in [5]. Since bubble dynamics becomes faster with increased initial liquid pressure, the results of Johnsen and Colonius apply also to the situations considered in this paper.

3.1.1. Pressure term \mathbf{X}_m^p

Following [4], the evolution of the interface is determined by the interface condition given by the solution of a two-material Riemann problem

$$\Re(\mathbf{U}_1, \mathbf{U}_2) = 0 \quad \text{on } \Gamma, \quad (16)$$

where \mathbf{U}_1 and \mathbf{U}_2 are the conservative variables for the first and second fluid, respectively. To obtain the momentum and energy exchanges across the interface, the Riemann problem is solved for the interface pressure p_i and the interface normal velocity \mathbf{u}_i in each cell that is cut by the interface. For problems with only weak or moderate shocks and expansion waves, simple non-iterative approximate Riemann solvers such as those of Toro [45] are sufficient, otherwise more accurate iterative solvers can be used. In this paper, the interface condition is obtained employing the Riemann solution of Hu and Khoo [46]

From the solution of the Riemann problem, the interface pressure p_i and the interface normal velocity \mathbf{u}_i serve to compute the term \mathbf{X}_m^p

$$\mathbf{X}_m^p = \begin{pmatrix} 0 \\ p_i \Delta\Gamma(\mathbf{n}_m \cdot \hat{i}) \\ p_i \Delta\Gamma(\mathbf{n}_m \cdot \hat{j}) \\ p_i \Delta\Gamma(\mathbf{n}_m \cdot \hat{k}) \\ p_i \Delta\Gamma(\mathbf{n}_m \cdot \mathbf{u}_i) \end{pmatrix}, \quad (17)$$

where \hat{i} , \hat{j} and \hat{k} are the unit vectors in x , y and z direction, respectively. Conservation is satisfied since $\mathbf{n}_1 = -\mathbf{n}_2$, i.e., the interaction

terms for the two fluids at the interface have the same magnitude but opposite sign.

3.1.2. Mass transfer term \mathbf{X}_m^t

For vapour–liquid interactions with phase change, mass transfer across the interface is modelled by \mathbf{X}_m^t . This term not only includes mass transfer across the interface, but also the appropriate momentum and energy exchange due to evaporation or condensation. The subscript m for differentiating between the two different fluids at an interface is $m = v$ for vapour and $m = li$ for liquid.

To model the phase change at the interface, we apply a thermal non-equilibrium assumption [47]. During the phase-change process, the pressure is in equilibrium at the vapour pressure and the temperature has a discontinuity at the phase interface. An expression for the rate of evaporation and condensation \dot{m} can be found in the book of Schrage [48]

$$\dot{m} = \frac{\lambda}{\sqrt{2\pi R_v}} \left(\frac{p_s(T_{li})}{\sqrt{T_{li}}} - \frac{p_v}{\sqrt{T_v}} \right). \quad (18)$$

Here, R_v is the specific gas constant in the vapour phase, and λ is the accommodation coefficient for evaporation or condensation (assumed to be constant), equal to the ratio of vapour molecules sticking to the phase interface to those impinging on it. T_v and T_{li} are the temperatures of vapour and liquid at the phase interface, respectively. p_v is the actual vapour pressure at the interface, and $p_s(T_{li})$ is the equilibrium (saturation) vapour pressure at temperature T_{li} and is obtained from the Clausius–Clapeyron equation

$$p_s(T_{li}) = p_0 \exp \left[\frac{L_v}{R_v} \left(\frac{1}{T_0} - \frac{1}{T_{li}} \right) \right], \quad (19)$$

where L_v is the latent heat of vapourization, and p_0 and T_0 are given by a reference saturation state. For our computations, we use $p_0 = 0.0234$ bar and $T_0 = 293$ K. With Eq. (18), the interface velocity induced by phase change is

$$\Delta q^* = \frac{\dot{m}}{\rho_{li}}, \quad (20)$$

where ρ_{li} is the density of the liquid at the interface. For cavitating flow, Δq^* is usually small and much smaller than the advection velocity of the interface [49], which suggests that the rates of pressure and temperature change due to the latent heat are insignificant. Therefore, one can assume that the phase change is much slower than the hydrodynamic interface interaction. As heat conduction in the bulk is also neglected, p_v , ρ_{li} , T_{li} and T_v are directly obtained from the solution of the Riemann problem (16).

In case of evaporation, i.e. $\dot{m} > 0$, the mass transfer from the vapour domain \mathbf{X}_v^t is expressed as

$$\mathbf{X}_v^t = \begin{pmatrix} \dot{m}\Delta\Gamma \\ \dot{m}\Delta\Gamma(\mathbf{u}_{li} \cdot \hat{\mathbf{i}}) \\ \dot{m}\Delta\Gamma(\mathbf{u}_{li} \cdot \hat{\mathbf{j}}) \\ \dot{m}\Delta\Gamma(\mathbf{u}_{li} \cdot \hat{\mathbf{k}}) \\ \dot{m}\Delta\Gamma \left(e_v + \frac{1}{2} |\mathbf{u}_{li}|^2 \right) + p_l \Delta q^* \Delta\Gamma \end{pmatrix}. \quad (21)$$

In case of condensation, i.e. $\dot{m} < 0$, it is

$$\mathbf{X}_v^t = \begin{pmatrix} \dot{m}\Delta\Gamma \\ \dot{m}\Delta\Gamma(\mathbf{u}_v \cdot \hat{\mathbf{i}}) \\ \dot{m}\Delta\Gamma(\mathbf{u}_v \cdot \hat{\mathbf{j}}) \\ \dot{m}\Delta\Gamma(\mathbf{u}_v \cdot \hat{\mathbf{k}}) \\ \dot{m}\Delta\Gamma \left(e_v + \frac{1}{2} |\mathbf{u}_v|^2 \right) + p_l \Delta q^* \Delta\Gamma \end{pmatrix}, \quad (22)$$

where \mathbf{u}_{li} and \mathbf{u}_v are the velocity vectors of liquid and vapour for the respective cut cell. e_v is the internal energy of vapour in this cell. The contribution to the mass transfer term from the liquid domain \mathbf{X}_{li}^t due to conservation is

$$\mathbf{X}_{li}^t = -\mathbf{X}_v^t. \quad (23)$$

Note that the change of internal energy in the liquid is small since the temperature variations due to phase change is negligible.

The accommodation coefficient λ of water has been extensively analyzed, and a range of values for λ can be found in the work of Marek and Straub [12]. Values are likely in the range of 0.001–1.0, thus we discuss the influence of different accommodation coefficients in Section 5.

3.2. Small cell mixing

The intersection between the immersed interface and the Cartesian grid can result in small cut cells for which a stable numerical integration based on the time step constraint of full cells cannot be achieved. As a more restrictive constraint may lead to prohibitively small time steps, a conservative mixing procedure is introduced, where the conserved quantities of such small cells are mixed with larger neighbour cells. The procedure follows that of Hu et al. [4]. Modifications are introduced in order to account for non uniform grid spacing and multiple spatial dimensions. The number of target cells adopted for the mixing is also increased and now includes all possible neighbour cells. The mixing procedure is applied only to cut cells with a volume fraction below a certain threshold, in our computations $\alpha_m = 0.6$. Increasing this threshold leads to a better numerical stability but at the same time results in larger numerical diffusion and vice versa.

Seven mixing target cells are determined from the local normal vector on the interface. For each mixing target cell a weight β_m is defined Fig. 2

$$\begin{aligned} \beta_m^x &= |\mathbf{n}_m \cdot \hat{\mathbf{i}}|^2 \alpha_{mix_{i,j,k}}, \\ \beta_m^y &= |\mathbf{n}_m \cdot \hat{\mathbf{j}}|^2 \alpha_{i,mix_{j,k}}, \\ \beta_m^z &= |\mathbf{n}_m \cdot \hat{\mathbf{k}}|^2 \alpha_{i,j,mix_k}, \\ \beta_m^{xy} &= \left| (\mathbf{n}_m \cdot \hat{\mathbf{i}}) (\mathbf{n}_m \cdot \hat{\mathbf{j}}) \right| \alpha_{mix_{i,j},mix_k}, \\ \beta_m^{xz} &= \left| (\mathbf{n}_m \cdot \hat{\mathbf{i}}) (\mathbf{n}_m \cdot \hat{\mathbf{k}}) \right| \alpha_{mix_{i,j},mix_k}, \\ \beta_m^{yz} &= \left| (\mathbf{n}_m \cdot \hat{\mathbf{j}}) (\mathbf{n}_m \cdot \hat{\mathbf{k}}) \right| \alpha_{i,mix_j,mix_k}, \\ \beta_m^{xyz} &= \left| (\mathbf{n}_m \cdot \hat{\mathbf{i}}) (\mathbf{n}_m \cdot \hat{\mathbf{j}}) (\mathbf{n}_m \cdot \hat{\mathbf{k}}) \right|^{2/3} \cdot \alpha_{mix_{i,j},mix_k} \end{aligned} \quad (24)$$

To avoid double mixing between two cells, the weighting factor is set to zero whenever a cell volume fraction is larger than that of the target cell. The weights are subsequently normalized to ensure consistency

$$\sum_{trg} \beta_m^{trg} = 1, \quad (25)$$

where trg stands for $trg = \{x, y, z, xy, xz, yz, xyz\}$.

The mixing flux \mathbf{M}_m^{trg} is calculated for each mixing direction in the following way:

$$\begin{aligned} \mathbf{M}_m^{trg} &= \frac{\beta_m^{trg}}{\alpha_m V \beta_m^{trg} + \alpha_{trg,m} V_{trg}} \\ &\quad \cdot [(\alpha_{trg,m} V_{trg} \bar{\mathbf{U}}_{trg,m}) \alpha_m V - (\alpha_m V \bar{\mathbf{U}}_m) \alpha_{trg,m} V_{trg}] \end{aligned} \quad (26)$$

Conservation is maintained by a flux formulation, consistent with non-uniform Cartesian grids

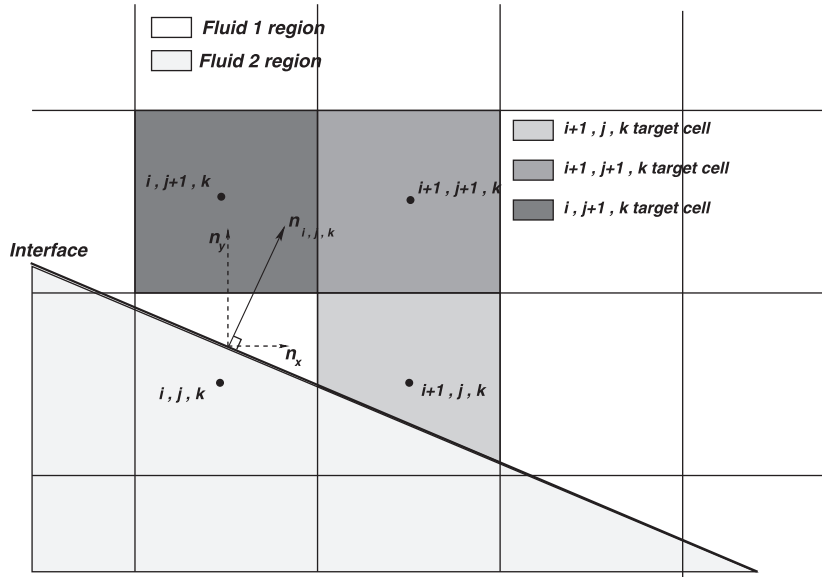


Fig. 2. 2D overview of mixing target cells.

$$\bar{\mathbf{U}}_m = (\bar{\mathbf{U}}_m)^* + \frac{\mathbf{M}_m^{\text{trg}}}{\alpha_m V} \quad (27)$$

$$\bar{\mathbf{U}}_{\text{trg},m} = (\bar{\mathbf{U}}_{\text{trg},m})^* - \frac{\mathbf{M}_m^{\text{trg}}}{\alpha_{\text{trg},m} V_{\text{trg}}} \quad (28)$$

where $(\bar{\mathbf{U}}_m)^*$ and $(\bar{\mathbf{U}}_{\text{trg},m})^*$ are the volume averaged conserved variables of the cut cell and of the target cell before mixing. This procedure is applied accordingly for all cut cells and mixing target cells at the end of each *Runge–Kutta* substep.

It is interesting to see how the present mixing procedure deals automatically with vanished and newly created empty cells. In the first case, the residual conservative quantities are all transported to the target cells, whereas for the second case the conservative quantities in a newly created small cell are derived directly from its target cells.

4. Model verification

4.1. One-dimensional Vapour–water interaction

We consider a 1D vapour–water interaction case, see also [50]. Over-saturated water vapour condenses under the influence of a pressure wave. Initially, as shown in Fig. 3a, both phases cover an interval of 2 cm. Vapour is on the left side and water on the right side, with the phase interface at the origin. Both phases are initially at rest and have a common temperature of 293 K. The initial vapour pressure is 93 mbar, corresponding to a saturation temperature of 343 K. The water pressure is 193 mbar. At the boundaries, we impose perfectly reflecting solid-wall conditions. The number of grid points is 200.

Fig. 3b shows the evolution of the phase interface with different accommodation coefficients $\lambda = 0, 0.075, 0.25, 0.5$ and 0.75 . One can find that without phase change ($\lambda = 0$), the water first expands due to its higher pressure and then shrinks and expands periodically as the generated pressure wave propagates back and forth in the liquid. Every impact of the pressure wave on the interface changes the direction of the interface motion. With phase change, the liquid volume still oscillates, but the interface location gradually moves into the vapour due to condensation of the over-saturated vapour. The expansion rate depends on the accommodation coefficient. At later times, the expansion slows down for large λ

due to a faster consumption of over-saturated vapour, and reaches a steady average position.

Fig. 4a plots the velocity profile at $t = 1$ ms. The velocity jump corresponds to the mass flux across the interface. With phase change, the pressure of both vapour and water decreases considerably (see Fig. 4b) as the over-saturated vapour is consumed.

4.2. Three-dimensional free vapour bubble collapse

The evolution of an empty spherical bubble in an incompressible liquid, without viscous effects and surface tension, is described by a modified form of the Rayleigh–Plesset equation [51]

$$R\ddot{R} + \frac{3}{2}\dot{R}^2 = \frac{p_L - p_{li}}{\rho_{li}}, \quad (29)$$

where R is the radius of the bubble, \dot{R} is the velocity of the bubble surface, \ddot{R} its acceleration, ρ_{li} the liquid density, p_{li} the liquid pressure at infinity, and p_L is the pressure of the liquid at the bubble surface. For analysis one assumes that the pressure at the surface is constant and equal to the saturation pressure of vapour, i.e. $p_L = p_{\text{sat}} = 2340$ Pa. Rayleigh [1] was the first to integrate this equation of motion to evaluate the bubble collapse time

$$t_{\text{Rayleigh}} \cong 0.915 R_0 \sqrt{\frac{\rho_{li}}{p_{li} - p_{\text{sat}}}}, \quad (30)$$

where R_0 is the initial bubble radius.

Following Sezal [52], we compare this analytical result with a numerical simulation of a vapour bubble at saturation pressure in water. A sketch of the setup is shown in Fig. 5a. The initial bubble radius is $R_0 = 0.4$ mm. We take advantage of symmetry and consider only one-eighth of the bubble in a domain with a length of 5 mm in all directions. The grid spacing is equidistant in the bubble region while grid stretching is applied in the far-field. We investigate three levels of refinement with 96, 48 and 24 computational cells spanning the initial bubble radius, representing the fine, medium and coarse grid, respectively. Following Niederhaus et al. [53], outlet boundary conditions are imposed at the far-field boundaries of the computational domain by setting gradients across the boundary to zero. Thus, reflections are minimized but not fully eliminated. The effect of reflections on the solution is minimized by placing the boundaries far away from the region of

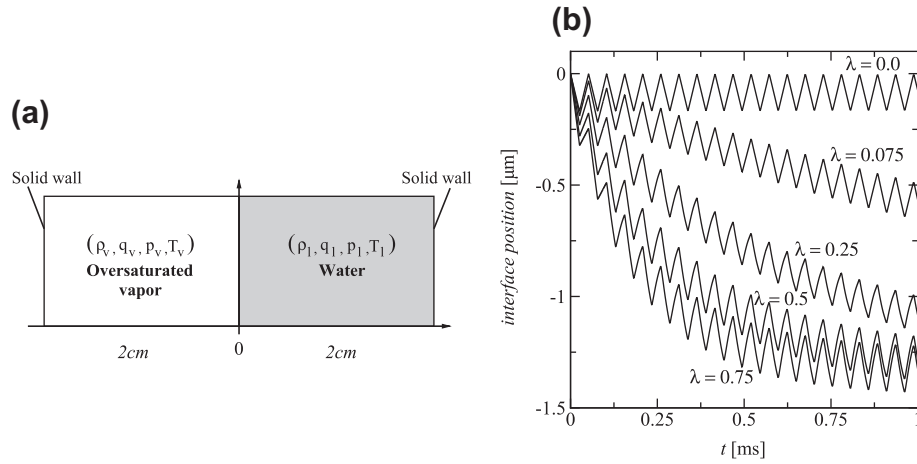


Fig. 3. One-dimensional vapour–water interaction: (a) Sketch of the problem and (b) evolution of the phase interface with different accommodation coefficients.

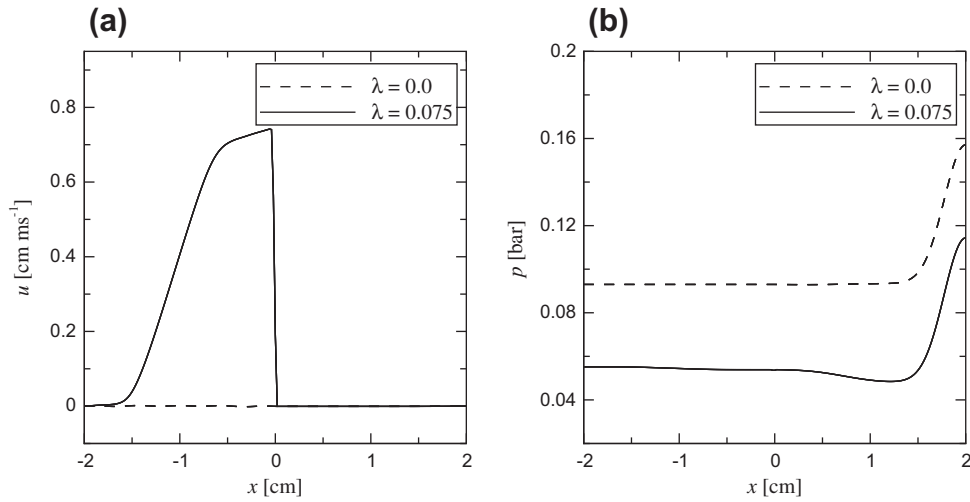


Fig. 4. One-dimensional vapour–water interaction: (a) Velocity and (b) pressure profiles at $t = 1 \text{ ms}$ for with and without phase change.

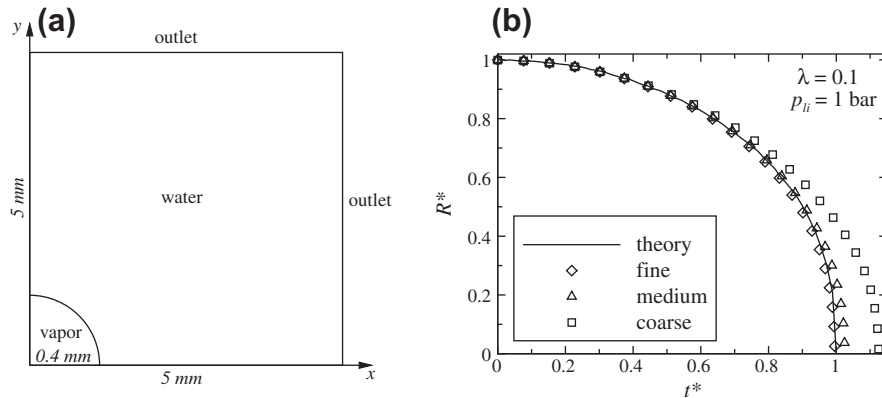


Fig. 5. Three-dimensional free vapour bubble collapse: (a) Sketch of the problem and (b) evolution of the normalized bubble radius $R^* = R/R_0$ with respect to normalized time $t^* = t/t_{\text{Rayleigh}}$.

interest. Compressibility is taken into account for both phases and the initial material states are:

vapour : $p = p_{\text{sat}} = 0.0234 \text{ bar}$, $T = 293 \text{ K}$,

water : $p = p_{li} = 1 \text{ bar}$, $T = 293 \text{ K}$.

Initial velocity is zero everywhere. The initial densities are given by the corresponding equation of state. The accommodation coefficient is set to $\lambda = 0.1$.

Fig. 5b shows the evolution of the normalized bubble radius $R^* = R/R_0$ over normalized time $t^* = t/t_{\text{Rayleigh}}$. The bubble radius

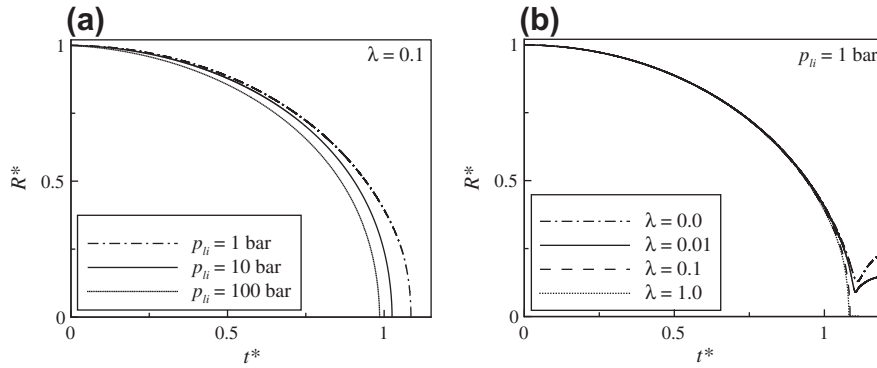


Fig. 6. Three-dimensional free vapour bubble collapse: Coarse-grid results to study the influence of (a) the compressibility of the liquid and (b) the non-equilibrium assumption.

R is calculated based on the bubble volume. We observe convergence, and the excellent agreement of the fine-grid results with the theory demonstrates the ability of our method to predict the collapse dynamics of a single bubble. Small differences at later times are in agreement with the computations of Sezal [52], and are most likely due to compressibility effects in the liquid that are not included within the theory and have also been observed in experiments [54]. This fact can be verified by studying the influence of the initial liquid pressure p_{li} . Coarse-grid results in Fig. 6a indicate that a higher initial liquid pressure, which leads to increased compressibility effects, results in an increasing deviation from theory at late stages of collapse.

Experimental investigations [17,55,56] demonstrate that under physical conditions, a vapour bubble generally rebounds after the first collapse. Following the numerical work of Akhatov et al. [56], the interface motion depends strongly on the thermodynamic non-equilibrium at the interface and on the amount of non-condensable gas inside the bubble. Fig. 6b provides the results of a coarse-grid study on the influence of the non-equilibrium assumption in our model. We see that, as in [56], small accommodation coefficients ($\lambda = 0.01, 0.0$) prevent the bubble from full collapse. The bubble rebound starts before the bubble radius reaches the size of a grid cell. However, when the accommodation coefficient is large enough ($\lambda = 1.0, 0.1$), the collapse depends primarily on the initial conditions. Non-condensable gas was not taken into account in our analyses.

5. Oscillating vapour bubble with phase change

The oscillation of a gas bubble in a liquid is a popular test case in the field of gas–liquid interaction e.g. [8–11]. Motivated by the observation in Fig. 6b, see previous section, we investigate the influence of the non-equilibrium phase change model on the oscillation of a three-dimensional free vapour bubble in more detail. Initial configuration is a vapour bubble of radius 160 μm in water where vapour pressure is much larger than water pressure. As shown in Fig. 7a, we consider only one-eighth of the vapour bubble in a domain with a length of 10 mm in all directions, exploiting sectional symmetries. The accommodation coefficient is varied between $0 \leq \lambda \leq 0.1$.

With three different levels of grid refinement corresponding to 40 (coarse), 80 (medium) and 160 (fine) cells in each direction, we quantify the level of numerical uncertainty. For all refinement levels, we use the same hyperbolic grid stretching $(1 - \tanh(\delta^* (1 - i/i_{\max}))) / \tanh(\delta)$ with $\delta = 1.05$. Fig. 7b gives an impression of the coarse grid and shows the initial size of the vapour bubble within the computational domain. The initial material states for this problem are

vapour : $p = 78,039$ bar, $\rho = 1.63$ g/cm³,
water : $p = 100$ bar, $T = 293$ K.

Initial velocity is zero everywhere. Initial vapour temperature and water density are given by the corresponding equations of state.

As the effect of the accommodation-coefficient variation on the overall bubble evolution does not depend significantly on the liquid pressure, we choose a rather large liquid pressure, unlike previous authors. For high water pressures, the time step constraint for the numerical scheme is relaxed, and the significantly reduced computational costs facilitate parameter analyses.

Results for the evolution of the bubble radius without phase change ($\lambda = 0.0$) on different grids are given in Fig. 8b. The vapour bubble initially grows due to large internal pressure until a maximum size of approximately 1.45 mm on the fine grid is reached. At this point the water pressure is already larger than the vapour pressure, initiating bubble collapse. An oscillatory process develops as the collapse is reversed when the vapour pressure reaches a critical value. Due to massive compression towards the final stage of the collapse, the bubble-radius growth rate is much larger for the small bubble than for the large bubble.

Comparing the results for different levels of grid refinement in Fig. 8b, we note that the oscillation amplitude and the period increase with increasing mesh resolution due to two different reasons. First, numerical dissipation is smaller at larger resolutions, and second, the better resolution of the initial bubble leads to a higher initial vapour mass on fine grids. We also observe that the relative error between two levels of grid resolution decreases strongly with increasing resolution, which is a consequence of the high-order discretization scheme.

For the medium grid the effect of varying λ is analysed (Fig. 8a). Increasing λ leads to a faster phase change and therefore to a stronger damping of the oscillation as vapour pressure is reduced due to condensation. Additionally, lower vapour pressures slightly decrease the period of one full oscillation cycle.

As mass for both phases is exactly conserved for $\lambda = 0.0$, the bubble radius oscillates around a constant average value (Fig. 8b). This average radius is reached for constant and equal inside and outside pressure $p_v = p_{li} = 100$ bar. The decay of the oscillation amplitude over time is in agreement with experimental [54] and numerical [57] observations. It is primarily related to the emission of shock waves and the accompanying entropy generation during the period of maximum compression [17].

The average value decreases continuously due to condensation as soon as the phase change model is used ($\lambda \neq 0.0$). For high accommodation numbers ($\lambda = 0.1, 0.05$) the bubble reaches the grid resolution limit already after a few oscillation cycles. The vapour is completely condensed and the bubble disappears

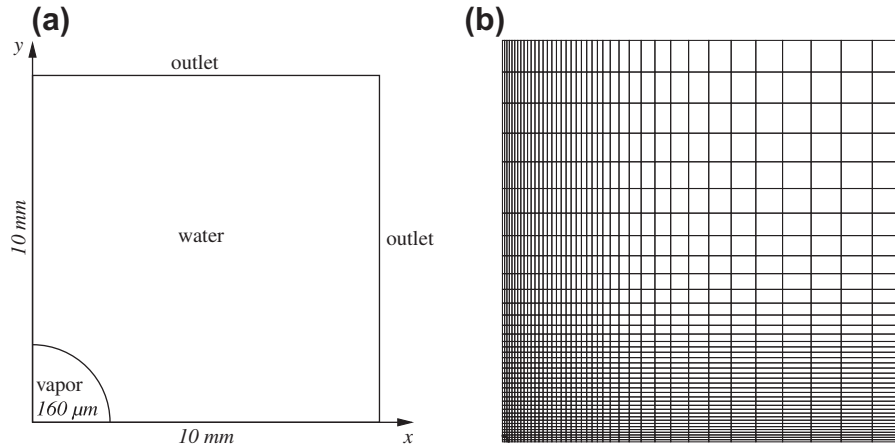


Fig. 7. Three-dimensional free vapour bubble oscillation: (a) Sketch of the problem and (b) two-dimensional view of the coarse grid with initial bubble radius shown in the bottom left corner.

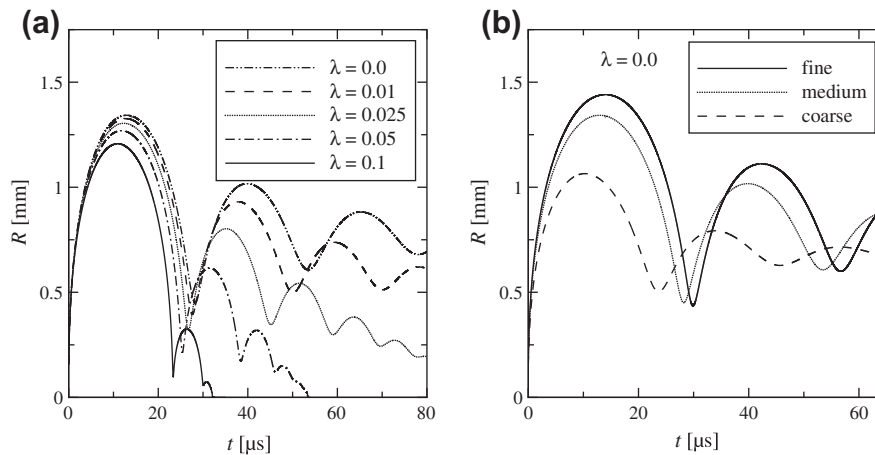


Fig. 8. Three-dimensional free vapour bubble oscillation: (a) Influence of the accommodation coefficient λ and (b) resolution study for zero-accommodation.

(Fig. 8a). For a moderate accommodation number (e.g. $\lambda = 0.025$) we see, that the bubble radius decreases slowly over time even though the bubble oscillation is hardly visible. This is an effect of the non-equilibrium assumption at the interface, leading to condensation of over-saturated vapour, even without oscillation.

The strong dependence of the results on the accommodation coefficient and the considerable uncertainty about the physical value of λ [12] point out the need for more detailed experimental investigations on the accommodation coefficient.

6. Collapse of a spherical vapour bubble near a solid wall

We investigate the collapse of a vapour bubble near a solid wall. As shown in Fig. 9, the initial bubble radius is $400 \mu\text{m}$. We take advantage of symmetries and compute only one-quarter of the bubble. Data are mirrored on the (X-Y)- and (Y-Z)-plane for visualization. The initial material states are:

vapour : $T = 293.0 \text{ K}$, $p = 0.02340 \text{ bar}$,

water : $T = 293.0 \text{ K}$, $p = 100.0 \text{ bar}$,

where the temperature is the saturation temperature corresponding to the initial vapour pressure. Both fluids are initially at rest, and densities are given by the corresponding equations of state. Since Marek and Straub [12] found that the accommodation coefficient decreases with increasing ambient pressure, it is taken as $\lambda = 0.01$.

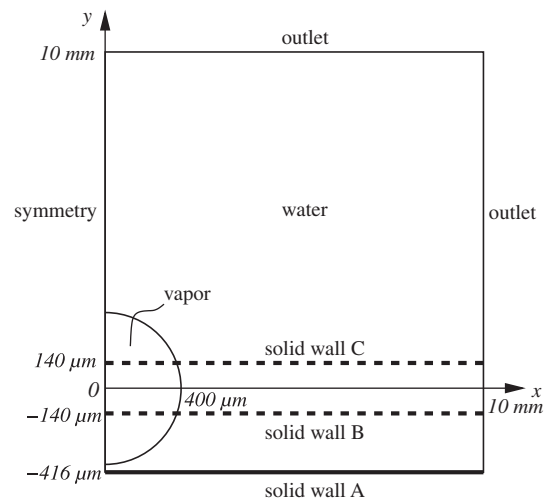


Fig. 9. Collapse of a spherical vapour bubble near a solid wall: Sketch of the problem. Three configurations A–C with different wall positions are investigated.

This test case is relevant for the collapse of cavitation bubbles near a solid structure, resulting in cavitation erosion. One objective of the simulations is to quantify the effects of re-entrant jet and full

bubble collapse on the wall pressure. As these effects are expected to be different for detached or attached bubbles, we consider three different wall positions A, B and C (see Fig. 9) in Sections 6.1, 6.2, 6.3. Although experimental investigations on vapour-bubble collapses generally consider atmospheric conditions, we deliberately assume a much larger ambient pressure as this situation is relevant for many technical applications involving liquid cavitation, most importantly high-pressure pumps for liquid-fuel injection currently operating with pressures up to 2500 bar [26]. By setting the initial liquid pressure in our simulations to 100 bar we can also assess whether experimental observations at low ambient pressures are valid at such high technically relevant pressures.

The grid spacing is equidistant in the bubble region with 100 computational cells per initial bubble radius. Grid stretching is applied in the far-field. Outlet boundary conditions are imposed at $x, y, z = 10$ mm. As boundary condition for the level-set at the wall, we use symmetry conditions. On coarse grids, a comparison with simulations using a linear extrapolation of the level-set across the wall showed only very small quantitative but no qualitative effects. Thus, we think that the level-set boundary condition at the wall as well as a potential contact angle due to surface tension are of minor importance.

6.1. Detached spherical vapour bubble

For the detached-bubble case, the wall is at position A (see Fig. 9), 416 μm from the bubble centre, i.e. there is a 16 μm gap between bubble and wall.

The initial configuration is shown in Fig. 10a. After 4.0 μs (Fig. 10c), the bubble volume has shrunk to approximately 1/20 of its initial size. The stand-off distance has not changed much, since there is a region of low water pressure in the gap between bubble and wall. A cavity has started to develop at the top, driven by a region of high water pressure above the bubble. At time $t = 4.2$ μs (Fig. 10d), the re-entrant jet is already fully developed. While the water pressure is high in the region above the vapour bubble and at the bottom of the cavity, we observe even negative pressures in the main field of the re-entrant jet caused by velocities up to more than 1100 m/s in this area. After 4.225 μs (Fig. 10e) the re-entrant jet impacts at the bottom of the vapour bubble and impinges onto the wall shortly afterwards (Fig. 10f). The pressure increases strongly and we observe wall pressures of more than 10,000 bar corresponding to more than hundred times the initial water pressure. A three-dimensional view of the bubble surface at this time instant is given in Fig. 10b, also showing the wall pressure field.

Strong pressure waves are reflected at the wall and travel back into the flow field. They interact with the remaining bubble ring and initiate the final bubble collapse (Fig. 10g and h). After the final collapse, the pressure increases (Fig. 10i). Although about the same pressure levels are reached as for the re-entrant jet hitting the wall (Fig. 10f), these maximum pressures occur at some distance away from the wall. It can be concluded that in case of collapse of a single detached vapour bubble at 100 bar ambient-pressure conditions, the highest potential for wall erosion is due to the impact of the re-entrant jet.

Later two rings of very low pressure develop in the water (Fig. 10j). The first one is attached to the wall, the second is detached. In these regions a rebound of the vapour bubble can occur. Such newly generated vapour bubbles can result in additional wall erosion when collapsing. As smaller distances of the rebound bubbles from the wall result in larger wall pressures, the attached low-pressure area is more important than the detached, even though the detached one has smaller pressure. Note that vapour bubble rebound is not explicitly considered as no nucleation model is employed.

6.2. Attached spherical vapour bubble cut by a wall in its lower hemisphere

For a bubble which is initially cut by the wall in the lower hemisphere at position B (see Fig. 9), 140 μm below the centre of the bubble, the initial situation is shown in Fig. 11a. Similar configurations have been experimentally investigated at atmospheric conditions by Tomita and Shima [16]. A strong expansion wave travels from the interface into the water. Upon the interaction with the wall, the liquid pressure is further decreased, leading to a lower pressure where the vapour bubble is attached to the wall than at its top. This changes the contact angle of the interface at the wall (Fig. 11c). At this time, also the pressure has increased above the bubble, leading to the formation of a re-entrant jet (Fig. 11d) which penetrates through the bubble towards the wall. The fully developed re-entrant jet reaches velocities of approximately 900 m/s, causing negative pressure in the centre of the jet (Fig. 11e), similarly as with the attached bubble.

When breaking through the bubble and impinging onto the wall (Fig. 11f), the re-entrant jet strongly decelerates. The pressure increases and we observe wall pressures around 14,000 bar. A circular pressure wave travels outwards and interacts with the remaining vapour bubble ring. At time $t = 4.008$ μs (Fig. 11g), a cavity between wall and bubble ring can be found at the inside of the ring. A fast liquid jet with velocities up to 1500 m/s develops, causing a further pressure drop in the jet region (Fig. 11h). A three-dimensional impression of the vapour bubble shape at this stage is given in Fig. 11b.

After impacting, the fast outward running liquid strongly decelerates due to the intruding liquid around the vapour ring (Fig. 11i). The pressure around the vapour ring increases to more than 16,000 bar and initiates the final collapse of the vapour ring (Fig. 11j).

At time $t = 4.093$ μs , the bubble is fully collapsed, indicated by high pressure regions with a maximum wall pressure of about 32,000 bar in Fig. 11k. A strong pressure wave travels towards the centre (Fig. 11l) leading to a strong compression of the liquid in the centre region. Near the wall, a maximum pressure of about 50,000 bar, corresponding to 500 times the initial water pressure, can be found (Fig. 11m). Fig. 11n shows the post-collapse flow field. The most important observation is the appearance of a negative-pressure ring attached to the wall. Vapour bubble rebound is likely to occur in this region, but can only be handled with a nucleation model, as mentioned above.

6.3. Attached spherical vapour bubble cut by a wall in its upper hemisphere

For the third scenario we consider a vapour bubble cut by a solid wall in its upper hemisphere by setting the wall at position C (see Fig. 9), 140 μm above the virtual bubble centre. While for the two previous wall positions, the initial stages of collapse are quite similar, this time a completely different development occurs. Given the initial configuration in Fig. 12a, again an expansion wave travels from the interface into the liquid. Now, however, the expansion waves do not travel towards the wall, and a weaker expansion can be expected in the near wall region than for case B. The consequence can be seen clearly in Fig. 12b. Close to the wall, the liquid pressure remains larger than at the top of the bubble and accelerates the collapse in this region. A cavity between wall and bubble develops with further increasing pressure at later times (Fig. 12c). This can be also seen in the three-dimensional visualization of the bubble surface in Fig. 12k).

After 2.8 μs , the vapour bubble deforms to a mushroom-like shape (Fig. 12d). Although we observe at this stage again jet velocities over 900 m/s, similarly as with cases A and B, the pressure in-

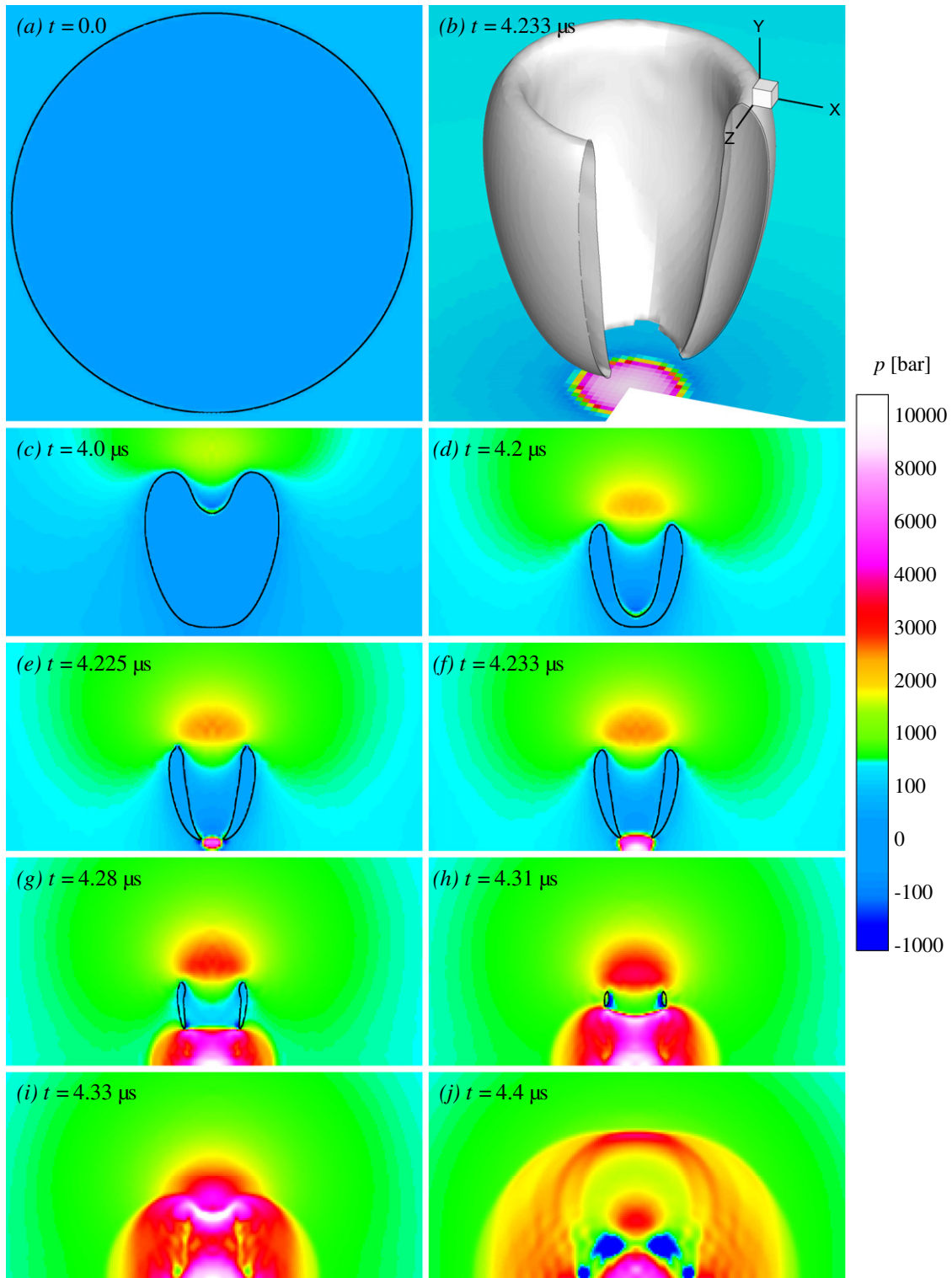


Fig. 10. Collapse of a vapour bubble in configuration A: (a) Initial configuration, (b) cut through an iso-surface of the zero level-set (interface) at $t = 4.0523 \mu\text{s}$, showing the shape of the bubble and the wall pressure, and (c–j) bubble shape and pressure field at different time instants. All figures except (b) have the same magnification scale.

side the cavity is comparatively large due to compression by the converging liquid area near the wall. Shortly before the vapour bubble detaches from the wall, the pressure reaches more than 5500 bar in regions with a liquid velocity of 950 m/s (Fig. 12e). At this time, the mushroom-like shape is well developed as can be seen in Fig. 12l. With incipient bubble collapse close to the wall,

water is compressed in the centre region. The pressure rises to more than 80,000 bar (Fig. 12f) corresponding to eight hundred times the initial water pressure or eight times the maximum wall pressure in the detached bubble case.

The inward rushing liquid is deflected in the centre region, and a fast jet develops from the wall towards the remaining bubble

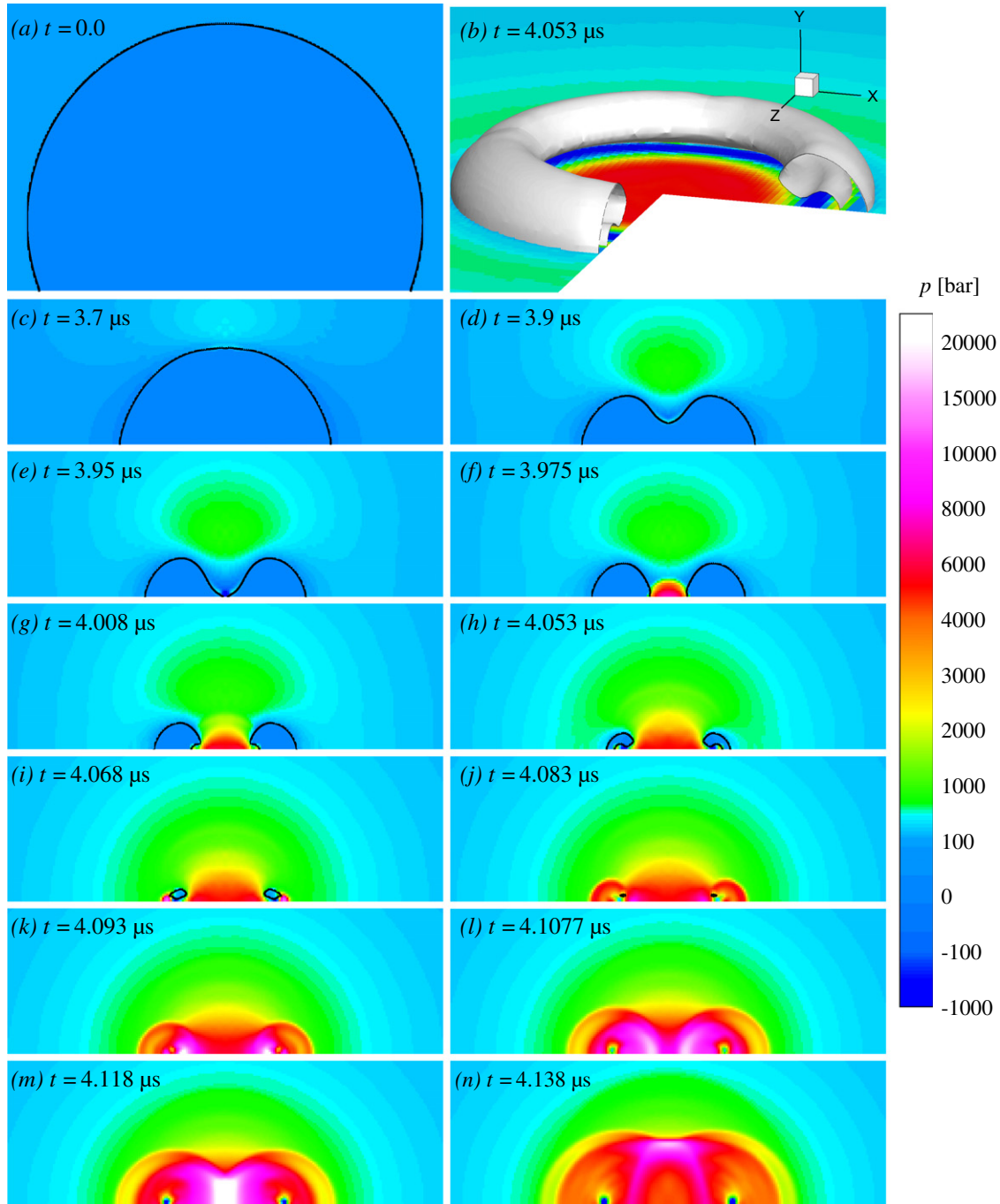


Fig. 11. Collapse of a vapour bubble in configuration B: (a) Initial situation, (b) cut through an iso-surface of the zero level-set (interface) at $t = 4.053 \mu\text{s}$ showing the shape of the bubble and the wall pressure, and (c–n) bubble shape and pressure field at different time instants. All figures except (b) have the same magnification scale.

fragment. Fig. 12g shows that the final collapse is mainly driven by this jet in the high pressure region below the bubble. As expected, the pressure increases again to approximately 50,000 bar when the rest of the vapour condenses (Fig. 12h). The areas with extreme pressure magnitudes are small and occur away from the wall. The pressure has already decreased to around 12,000 bar when the emitted shock wave impinges on the wall (Fig. 12i).

Rebound of the vapour bubble is likely to occur in a ring-shaped negative-pressure region, which we observe at later times (Fig. 12j). Since this low-pressure ring is comparably far away from the wall, the effect of potentially generated cavitation bubbles on the wall pressure would be rather small.

6.4. Discussion of the spherical configurations A–C

In general there are two different mechanisms leading to pressure jumps during a vapour-bubble collapse close to a solid wall: (i) fast deceleration of a liquid jet, (ii) release of a shock wave upon final bubble collapse. For the investigated configurations, the vapour bubble shrinks slowly during the initial period. The rapid stage of the bubble collapse starts with the development of a cavity, followed by the formation of a liquid jet. Pressure waves emitted during jet impact strongly affect the further bubble evolution.

Two fundamentally different scenarios at the early stages of bubble collapse can be found. For a detached bubble or a bubble

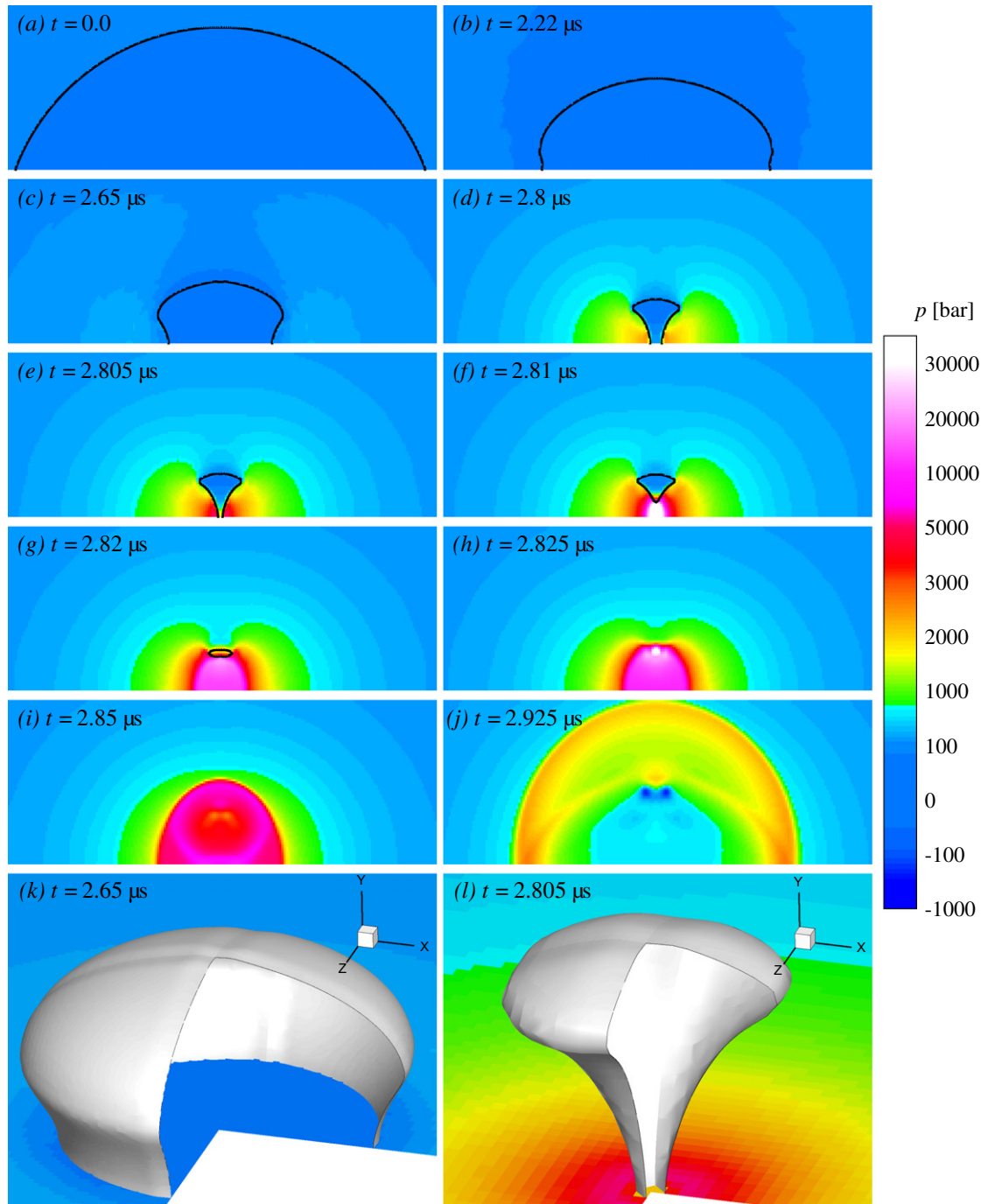


Fig. 12. Collapse of a vapour bubble in configuration C: (a–j) Bubble shape and pressure field at different time instants at same magnification scale, and (k and l) two cuts through an iso-surface of the zero level-set (interface) at $t = 2.65 \mu\text{s}$ and $t = 2.805 \mu\text{s}$ showing the shape of the bubble and the wall pressure.

cut in the lower hemisphere, the collapse is initiated at the top of the bubble (Fig. 13a and b). A fast liquid re-entrant jet develops and penetrates through the bubble in wall-normal direction (Fig. 14a and b). For an attached bubble cut in the upper hemisphere, the collapse is initiated between wall and interface (Fig. 13c) and a liquid jet develops radially towards the bubble centre (Fig. 14c). These two scenarios were also found by Shima and Nakajima [37] in their investigation of the collapse of non-hemispherical bubbles attached to a solid wall.

The appearance of a secondary jet can be only observed with configuration B since the wall normal re-entrant jet is deflected at the wall and interacts with the remaining bubble ring

(Fig. 14b dashed lines). This secondary jet is radially symmetric and develops from the symmetry axis outwards in wall-parallel direction. For configuration A no secondary jet develops as the residual bubble ring is not attached to the wall.

The first occurrence of extreme pressure magnitudes coincides with jet impact. For cases A and B with a wall-normal re-entrant jet, the observed maximum wall pressures are of comparable magnitude (Figs. 10f and 11f). Slightly smaller values for the detached bubble can be attributed to the thin layer of liquid between bubble and wall, interacting with the re-entrant jet before wall impact. Looking at wall-parallel radial jets, one has to distinguish between the outward-pointing secondary jet of configuration B and the in-

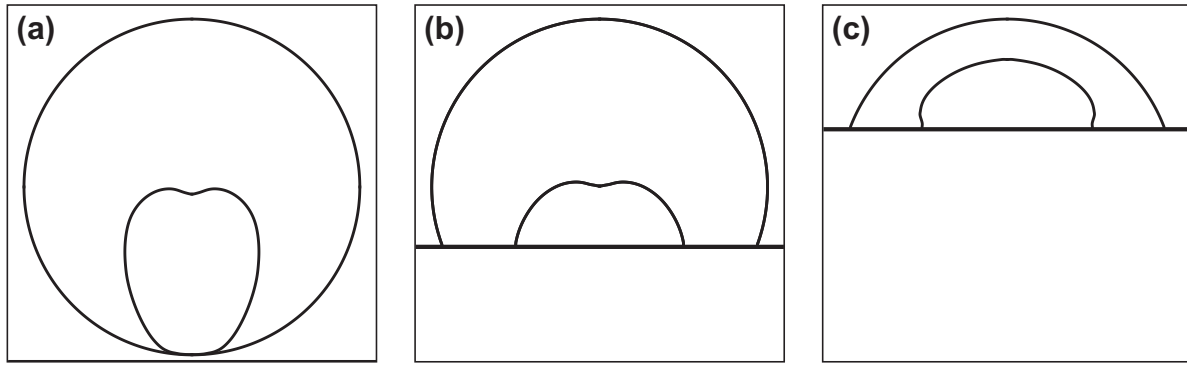


Fig. 13. Initial situation and bubble shape after cavity development for configurations A–C.

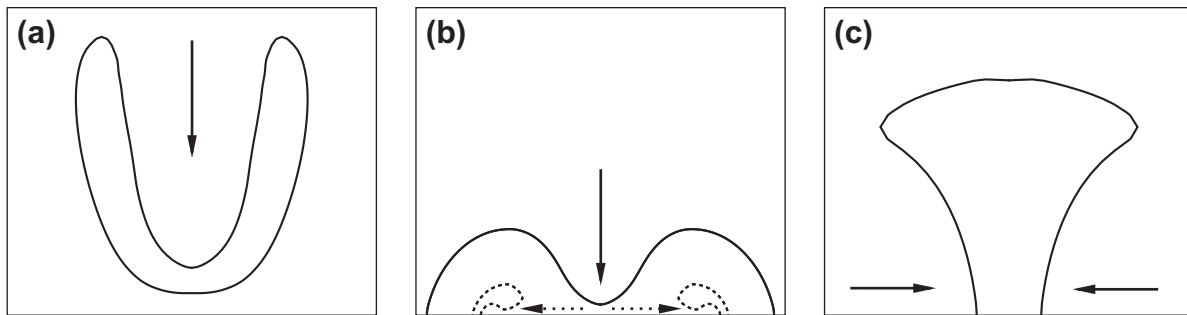


Fig. 14. Sketch of liquid jets during vapour bubble collapse near a wall: (a) Wall-normal re-entrant jet for configuration A, (b) primary wall-normal re-entrant jet (solid) and secondary wall-parallel outward pointing jet (dashed) for configuration B, and (c) wall-parallel inward pointing jet for configuration C. Arrows indicate the jet direction. Figures are not to scale.

ward pointing primary jet of configuration C. In the latter case, the liquid is gradually compressed while being transported towards the symmetry axis, where maximum pressure occurs. The maximum pressure after inward-pointing, wall-parallel jet impact is about eight times larger than that for a wall-normal jet (Fig. 12f). For the outward-running, wall-parallel secondary jet of configuration B, extremely low pressure is observed inside the jet (Fig. 11h) as an expansion of the liquid further decreases the pressure of the high-velocity jet. After jet impact, the liquid pressure is large, but significantly smaller than for the inward-pointing jet (Fig. 11i).

During the final stage of the bubble collapse, two different scenarios occur. For cases A and C, the residual vapour bubble after jet impact is detached and a high pressure region has developed between wall and bubble (Figs. 10f and 12f). Thus, the further collapse evolves from the bubble region that faces the wall. The pressure peak due to final bubble collapse occurs away from the wall (Figs. 10i and 12h). The emitted shock wave impinges on the wall with reduced magnitude, and the wall pressure does not reach the level observed for jet impact. The second scenario can be found for configuration B. After primary and secondary jet impact, a residual vapour ring remains at the wall. This ring is surrounded by high pressure which initiates the final collapse radially towards the symmetry axis (Fig. 11i). Liquid is compressed towards the centre region resulting in large pressure with maximum at the symmetry axis (Fig. 11m).

The occurrence of two successive wall-pressure peaks during the collapse of a wall-attached spherical vapour bubble, where the second one is larger, was identified experimentally by Tong et al. [21], who claim that the double peak is related to splashing and shock wave emission during collapse. However, in our simulations we do not observe splashing. An explanation may be that our bubble is directly attached to the wall whereas a small liquid film between bubble and wall exists in the experiment. Our results

indicate that the double peak can also be related to the impingement of the liquid jet and the emission of shock waves following the collapse of the remaining vapour ring. For detached bubble collapse, only one incident of large wall pressure was found experimentally and numerically. To the knowledge of the authors, there is no experiment dealing with the collapse of a bubble cut by the wall in its upper hemisphere (configuration C).

Fig. 15 shows the maximum wall pressure as a function of the non-dimensional initial stand-off distance L_0/R_0 , where L_0 is the distance from the wall to the initial bubble centre and R_0 is the initial bubble radius. It is evident that a more symmetric event leads to larger pressure and that a wall cutting through the upper hemisphere of a bubble ($L_0/R_0 < 0$) may be more critical for cavitation erosion, although the initial bubble volume is smaller.

The collapse of a hemispherical bubble attached to the wall is equivalent to the free, spherically symmetric collapse of a full bubble (Fig. 16a). In our simulations, we find a maximum wall pressure of about 470,000 bar shortly before the bubble becomes smaller than the minimum numerical cell size (Fig. 16b), which is one order of magnitude larger than for configurations A–C. This very large pressure is physically reasonable as Vogel et al. [17] estimated a maximum pressure of 60,000 bar inside a bubble of radius 50 μm at atmospheric ambient conditions shortly before the rebound. Ohl et al. [55] found that for the same initial diameter the minimum bubble radius is even less than 36 μm , indicating that the pressure inside the bubble is even higher. As their investigations were performed under atmospheric conditions, following Eq. (30) the collapse at 100 bar ambient pressure is approximately ten times faster, thus here the maximum pressure should be about one order of magnitude larger than in the experiments.

For attached vapour bubbles cut by the wall in the lower hemisphere, the maximum wall pressure decreases with increasing stand-off distance when the re-entrant jet begins to dominate

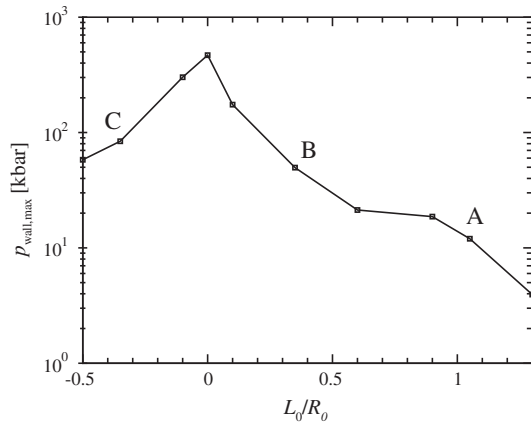


Fig. 15. Maximum wall pressure as a function of the non-dimensional initial stand-off distance L_0/R_0 . Configurations A–C are marked.

the evolution. At $L_0/R_0 \lesssim 1$ the maximum wall pressure is already equal to the pressure after jet impact. If the bubble is detached ($L_0/R_0 > 1$), the liquid film between bubble and wall damps the re-entrant jet before impingement and the maximum wall pressure strongly decreases (Fig. 15).

Experiments at atmospheric conditions [16] show that the maximum wall pressure increases strongly around $L_0/R_0 = 1.2$. They claim that at a higher stand-off distance, the rebound of the bubble occurs before the re-entrant jet impacts and, thus, the emitted shock wave impacts before the liquid jet. In the present study, we do not observe such a behaviour. The initial liquid pressure of

100 bar results in a stronger compression of the vapour bubble to a much smaller minimum volume. For all investigated bubble wall configurations, the liquid jet has enough time to develop and jet impact always precedes bubble rebound. The pressure increase takes place at a large stand-off distances, where the bubble collapse is of no practical relevance concerning wall erosion. This finding is very important since it shows that quantitative estimates obtained at atmospheric ambient pressure cannot be directly transferred to high pressure conditions although the general collapse mechanisms are very similar [16,17].

Experiments [3] show vapour-bubble rebound after final collapse. As we do not employ a nucleation model, we cannot consider rebound explicitly but areas where rebound is likely to occur can be identified from negative pressures in the post-collapse flow field. For wall erosion, rebound can be important as newly created vapour bubbles collapse again and can lead to further damage. Johnsen and Colonius [5] show that the maximum wall pressure after a bubble collapse depends strongly on the initial stand-off distance of the bubble. We have demonstrated that the collapse of attached bubbles can lead to even larger wall pressure. A bubble rebound far away from the wall, as can be expected to occur for configuration C (Fig. 12j), is less relevant. However, for cases A and B, bubble rebound probably occurs near the wall and may be critical (Figs. 10j and 11n).

Since the zone of potential rebound after the collapse of a bubble at configuration B is ring-shaped, the erosion pattern resulting from the collapse of rebounded vapour bubbles would be approximately circular. Such erosion patterns have been observed in experiments [16,18]. Another explanation for experimentally observed circular damage patterns is an asymmetric collapse of the

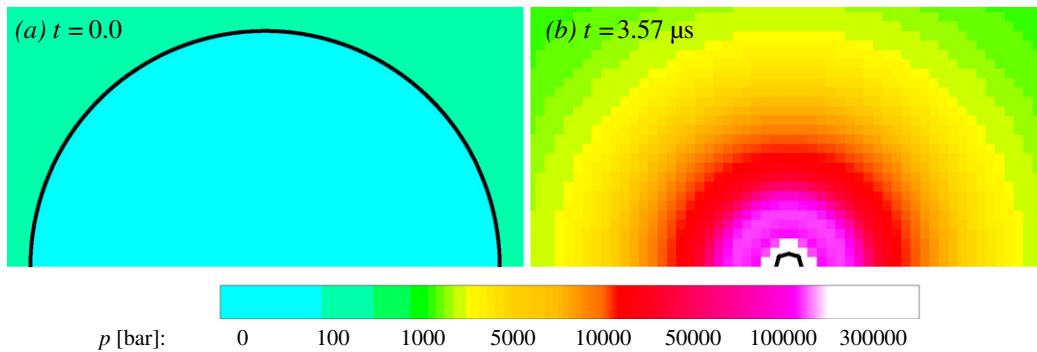


Fig. 16. Collapse of a hemispherical vapour bubble near a solid wall: (a) Initial configuration and (b) pressure field shortly before final collapse with a 400% magnification. The scenario is equivalent to the collapse of a free spherical vapour bubble.

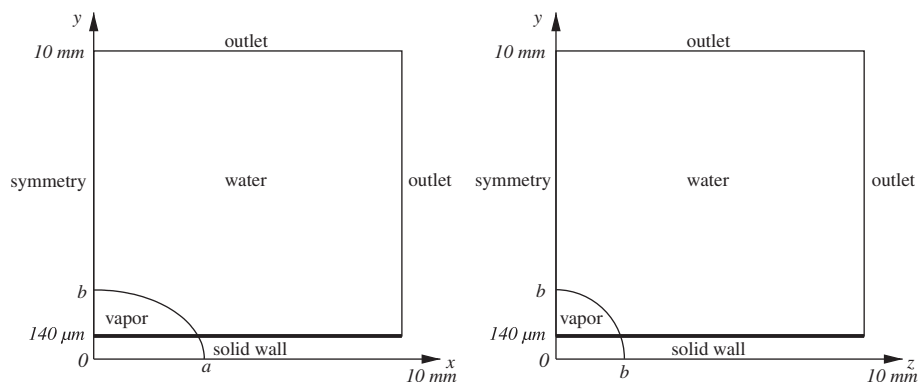


Fig. 17. Collapse of an ellipsoidal vapour bubble attached to a solid wall: (x, y) and (z, y) sketch of the problem. The length of the semiaxis $a = 3/2R_{\text{sphere}}$ and $b = \sqrt{2/3}R_{\text{sphere}}$ are taken in such a way that the volume of the ellipsoid fits the volume of a sphere with radius $R_{\text{sphere}} = 400 \mu\text{m}$.

vapour ring after jet impact. Stability analyses of the bubble shape [49] indicate instability at late stages of a collapse. Small deviations from the ideal shape, that are inevitable in the experiment, thus can produce an asymmetric collapse and prevent the axially symmetric final compression of the liquid in the centre region. The influence of an initial shape asymmetry is investigated in Section 7.

Final stages of bubble collapse with an inviscid sharp-interface model cannot be grid independent as the numerical grid size defines the smallest resolved physical length scale of the flow. Increasing the grid refinement therefore also increases the range of resolved details of the interface evolution. This becomes clear when considering the spherically symmetric case of a free va-

pour-bubble collapse. Since the bubble remains perfectly spherical, the grid spacing would have to be infinitesimally small to resolve the final collapse. However, coarse-grid results confirm that our simulations capture accurately flow and bubble evolution up to such singular events.

Due to the strong velocity gradients in the liquid jets and at the wall, an effect of viscosity cannot be fully excluded at the late collapse stages. Since the Reynolds number for our set-up is much higher than the critical Reynolds number found by Popinet and Zaleski [30] (see Section 3.1), only small overpredictions of the maximum pressure and jet velocity but no qualitative implications are likely.

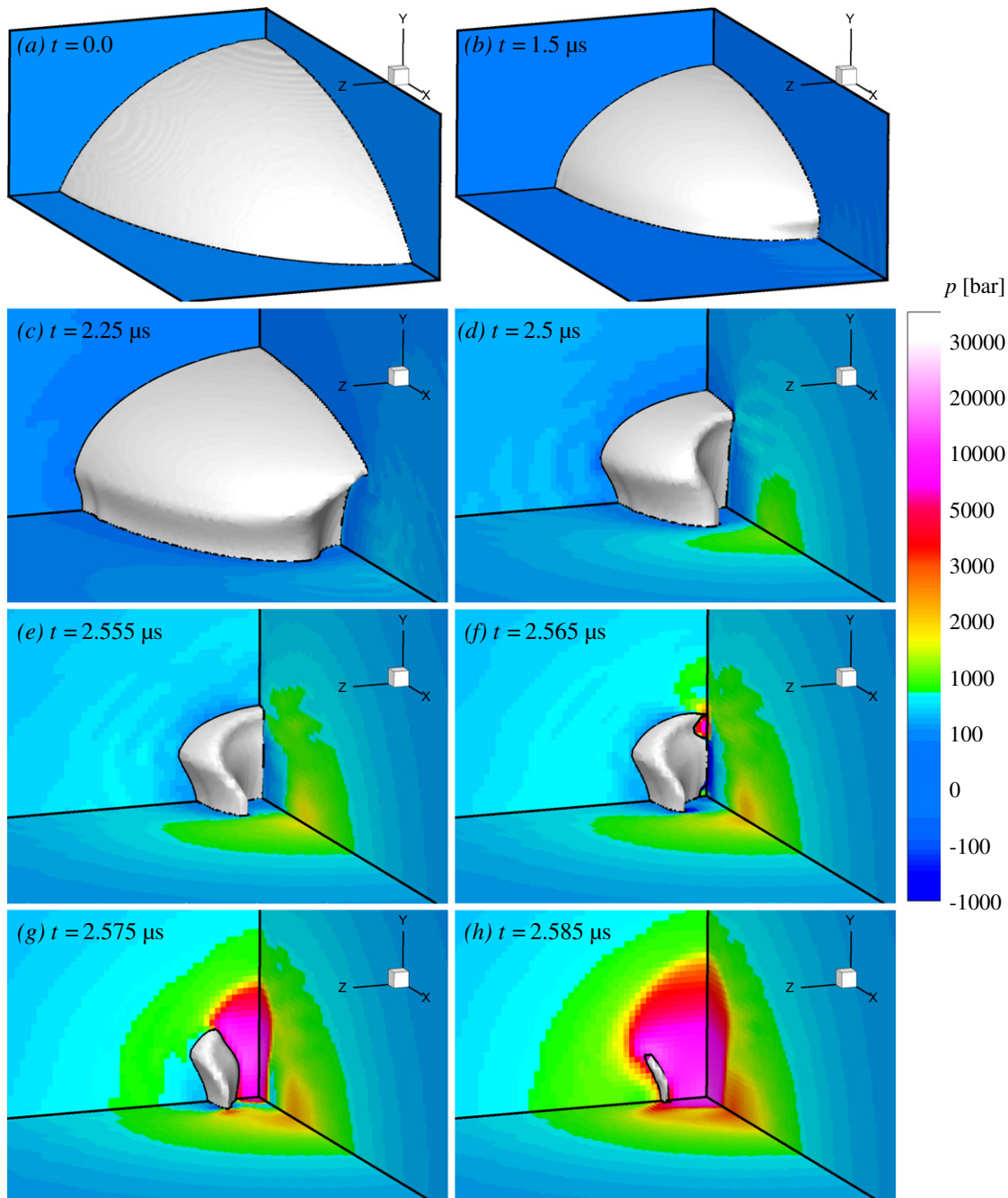


Fig. 18. Collapse of an ellipsoidal vapour bubble attached to a solid wall: Pressure fields at the symmetry planes and the wall and iso-surfaces of the zero level-set demonstrate the time evolution. Figures (c–h) are plotted with twofold magnification as compared to (a and b).

7. Collapse of an ellipsoidal vapour bubble attached to a solid wall

The ideal situation of spherical vapour bubbles hardly applies to technical applications, where cavitation bubbles are most likely non-spherical. A moderate increase of geometrical complexity by considering an ellipsoidal vapour bubble near a solid wall allows for an initial estimate on the effect of geometry variations on the bubble collapse. As it was found previously that configuration C of a spherical vapour bubble leads to the largest wall pressure, we consider a similar configuration with the ellipsoidal bubble (see Fig. 17). The equivalent full (non-cut) ellipsoid is rotationally symmetric about the x-axis and has the same volume as the spherical bubble of the previous section. We set the length of the semi-

major axis to $a = 3/2R_{\text{sphere}} = 600 \mu\text{m}$, where $R_{\text{sphere}} = 400 \mu\text{m}$ is the initial radius of the corresponding sphere. The volume is kept constant by choosing $b = \sqrt{2/3}R_{\text{sphere}} \approx 326.6 \mu\text{m}$ as the length of the semiminor axis. We use the initial material states given in Section 6 and similar grid spacing. Again, only one quarter of the problem is simulated due to sectional symmetry of the setup. For presentation, data are extended to the full domain.

Note that for the spherical-bubble collapse, it was found that the initial contact angle between interface and wall is relevant for the collapse process. For the ellipsoidal bubble the contact angle varies along the circumference (Fig. 18a). Where the contact angle is small, we expect weak expansion and therefore strong acceleration of the interface. As the contact angle is always below 90° the overall behaviour resembles that of configuration C

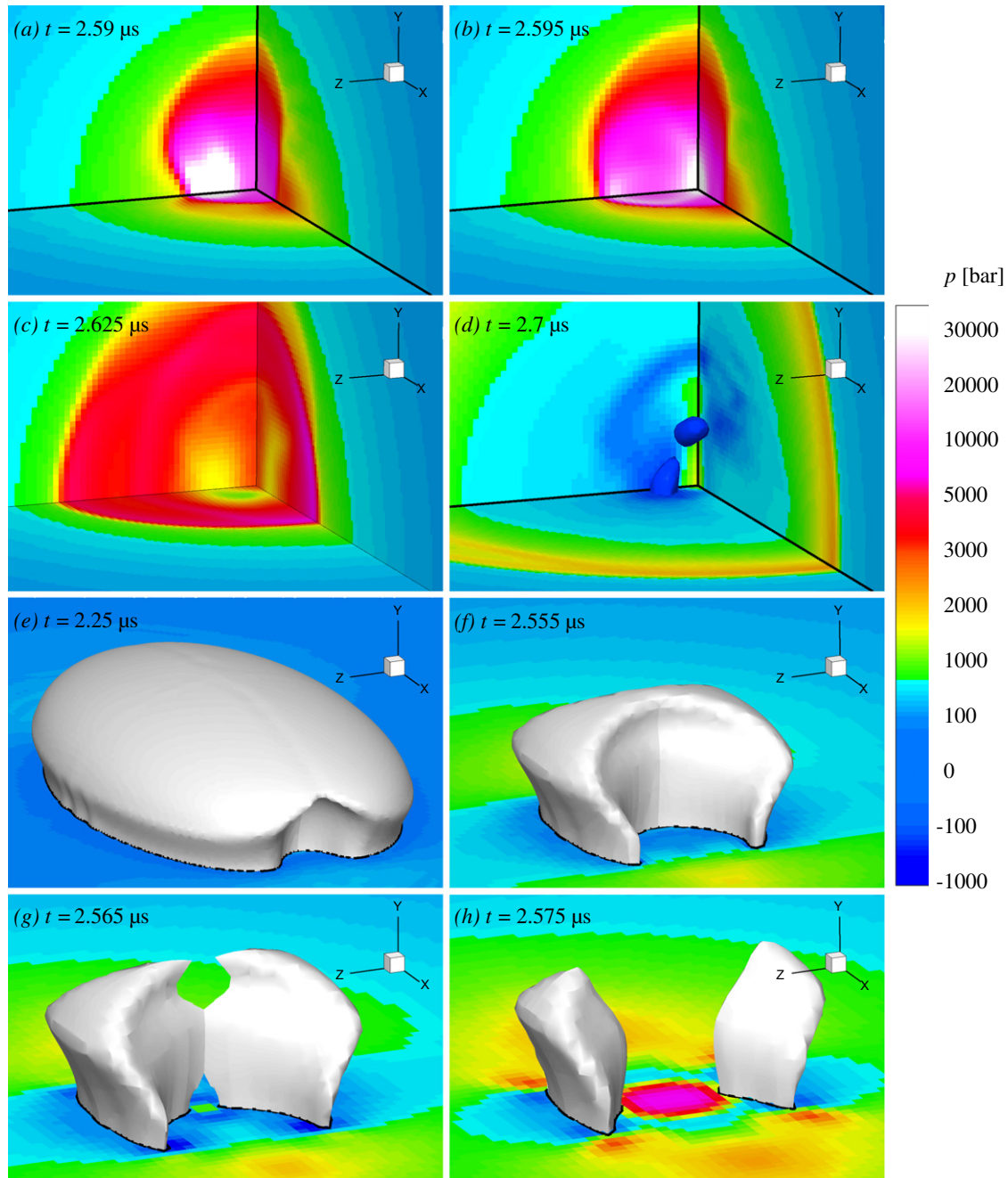


Fig. 19. Collapse of an ellipsoidal vapour bubble attached to a solid wall: (a–d) Development of the pressure field after the final bubble collapse. An additional iso-surface with pressure $p = -250$ bar is shown in (d). (e–h) Iso-surfaces of the zero level-set at different times indicate the shape of the bubble.

(Fig. 18b). Along the semimajor axis with smallest contact angle, bubble collapse has started already.

Fig. 18c shows that now, we can identify two different wall-parallel jets. The first jet corresponds to that found already for the spherical bubble in Section 6.3. This rotationally symmetric jet leads to a cavity between wall and interface along the circumference of the bubble. As a result the contact angle increases to values larger than 90° . The second jet is a consequence of the initial asymmetry. It penetrates into the bubble along the semimajor axis, similarly as a wall-parallel re-entrant jet. At this time, this second liquid jet is completely surrounded by vapour as can also be seen for the full problem visualization in Fig. 19e. It dominates the further bubble collapse as its velocity is larger than that of the first jet. The formation of a liquid jet from the point of maximum bubble extension during the collapse of non-spherical vapour bubbles is in agreement with results of Shima and Nakajima [37] and Dabiri et al. [58].

After $t = 2.5 \mu\text{s}$ (Fig. 18d), the dominating axial jet has penetrated deeper into the bubble and has slightly increased its cross section. Since the bubble has also become smaller, the jet now extends beyond the bubble surface. Figs. 18e and 19f show the situation at time $t = 2.555 \mu\text{s}$ shortly before the jet impact. The axial jet has fully developed, and we observe jet velocities up to 900 m/s. The circular jet deforms the vapour bubble into a mushroom shape that was observed already for the spherical bubble. The velocity of this jet is about 400 m/s.

The axial jet impacts in the bubble area at the wall and close to the top of the bubble (Fig. 18f). The full problem visualization in Fig. 19g shows more clearly that two bubble fragments are generated which, at that time, are still connected. When the axial jet impacts after full separation of the two bubble fragments (Figs. 18g and 19h), the pressure increases rapidly to more than 10,000 bar within the (y,z) symmetry plane, and the wall pressure reaches about 8000 bar. The high pressure between the two bubble fragments initiates the collapse of the residual vapour bubble (Fig. 18h).

The maximum wall pressure is reached at final collapse after $t = 2.59 \mu\text{s}$ (Fig. 19a). With more than 75,000 bar, the wall pressure is of similar magnitude as for the spherical bubble. The emitted shock wave leads to a compression in the centre region and a wall pressure of approximately 35,000 bar (Fig. 19b). After maximum compression, the liquid expands again. Areas of lower pressure start to build up (Fig. 19c). At later times, we observe negative pressures in the flow field close to the wall. The iso-surfaces in Fig. 19d show regions of liquid pressure below -250 bar, indicating potential vapour-bubble rebound, which corresponds to the final stages of spherical bubble collapses.

A comparison of results for the spherical configuration C and the ellipsoidal bubble shows that the maximum wall pressure, and thus the potential of wall erosion, is of similar magnitude, although the evolution of bubble collapse is quite different. Different is also the point of maximum wall pressure away from the symmetry axis for the ellipsoidal bubble, leading to a different wall-erosion pattern. An important finding for the post-collapse flow dynamics is the generation of low pressure regions close to the wall for the ellipsoidal case (Fig. 19d). A rebound of vapour bubbles is likely to occur in these regions leading to additional erosion. Note that after the collapse of the spherical bubble, negative pressure can only be found away from the wall (Fig. 12j).

8. Conclusions

In many technical applications involving the processing of liquids at large pressure differences, complex cavitation structures arise. If cavitation bubbles collapse near a solid surface, wall erosion is likely to occur. A first step towards controlling the cavita-

tion damage requires a comprehensive understanding of the underlying fundamental bubble-collapse mechanisms. For this purpose, generic configurations with spherical bubbles have been investigated. Since earlier experimental and numerical studies did not consider larger initial liquid pressures which are relevant for technical applications such as turbo-machinery and liquid-fuel injection nozzles, the objective of the present work is to investigate bubble collapse at 100 bar ambient pressure.

Experimental investigations of bubble-collapse mechanisms face several difficulties since lengthscales and timescales are in the range of micrometres and microseconds, respectively, or even smaller. Ideal initial configurations are difficult to reproduce (in particular non-spherical bubbles and small stand-off distances), and disturbances of the ideal shape can never be fully avoided. In experimental investigations of attached bubbles, the process of attachment at the wall often occurs while the collapse is already in progress, leading to an additional splashing effect that affects further bubble dynamics. An accurate determination of exact data (peak pressure, jet velocity) is still beyond current experimental capabilities.

In contrast, the major challenge for numerical investigations is to reproduce accurately the dynamics of the interface between water and vapour during the entire collapse process, including the high-speed dynamics of the late stages, where compressibility of both phases plays a decisive role. Due to the very small timescales, water and vapour are in non-equilibrium at the interface, which has to be taken into account by a numerical model. Our numerical sharp-interface method copes with these problems by solving the compressible Euler equations for water and vapour, and by coupling both phases with an interface-interaction term in a conservative way. The effect of evaporation and condensation is taken into account by a non-equilibrium phase-change model based on an accommodation coefficient λ .

The importance of the non-equilibrium assumption is apparent from our first results for an oscillating vapour bubble. Increasing λ leads to a significantly different behaviour. Oscillation amplitude and period were reduced, and in addition to the oscillation, we observe a continuous decrease of the bubble radius until the vapour is fully condensed.

In a second study, we have investigated the significance of the initial stand-off position of a bubble with respect to a wall for the bubble-collapse mechanisms at 100 bar initial liquid pressure. We have considered three different spherical-bubble-wall configurations. In case of a detached bubble and a bubble cut by the wall in its lower hemisphere, a wall normal re-entrant jet forms that leads to high wall pressures when interacting with the wall. In the second scenario an additional outward running jet develops after the impact of the re-entrant jet, and a further increased wall pressure is observed after the impact of the secondary jet and the upcoming final bubble collapse. For the detached vapour bubble, the final bubble collapse plays a minor role concerning wall pressure. If the wall cuts initially through the upper hemisphere, a circular cavity is created between wall and bubble surface and an inward-pointing wall-parallel jet forms. The impact of this radial jet leads to much higher wall pressures than the impact of a re-entrant jet.

The significance of bubble shape variation has been investigated by considering an ellipsoidal vapour bubble cut by the wall in its upper hemisphere. In addition to the radial jet, we found an axial, wall-parallel jet penetrating into the bubble from the point of maximum extension. This second jet dominates the collapse and leads to essentially different dynamics. Nevertheless, the maximum wall pressure, and along with it the potential of wall damaging, is of similar magnitude as for the corresponding spherical configuration. Thus, the bubble stand-off distance is of major importance concerning wall erosion.

After the final collapse, vapour-bubble rebound is likely to occur, but not explicitly considered here as a nucleation model is not employed. However, we can predict areas with a high probability of bubble rebound as our simulations exhibit low-pressure regions in the post-collapse flow field. This is an important observation since secondary bubble collapse can contribute to wall erosion.

We have demonstrated that numerical simulation allows to study in an ideal setting parameter ranges that are difficult to achieve experimentally (large initial liquid pressure, non-spherical configurations).

Acknowledgements

Financial support has been provided by the German Research Council (Deutsche Forschungsgemeinschaft – DFG). Computational resources have been provided in large part by the Leibniz Rechenzentrum Munich. The first author is member of the Technische Universität München (TUM) Graduate School.

References

- [1] Rayleigh L. On the pressure developed in a liquid during the collapse of a spherical cavity. *Philos Mag* 1917;34:94–8.
- [2] Kornfeld M, Suvorov L. On the destructive action of cavitation. *J Appl Phys* 1944;15:495–506.
- [3] Lindau O, Lauterborn W. Cinematographic observation of the collapse and rebound of a laser-produced cavitation bubble near a wall. *J Fluid Mech* 2003;479:327–48.
- [4] Hu XY, Khoo BC, Adams NA, Huang FL. A conservative interface method for compressible flows. *J Comput Phys* 2006;219:553–78.
- [5] Johnsen E, Colonius T. Numerical simulations of non-spherical bubble collapse. *J Fluid Mech* 2009;629:231–62.
- [6] Szeri AJ, Storey BD, Pearson A, Blake JR. Heat and mass transfer during the violent collapse of nonspherical bubbles. *Phys Fluids* 2003;15(9):2576–86.
- [7] Fedkiw R, Aslam T, Merriman B, Osher S. A non-oscillatory Eulerian approach to interfaces in multimaterial flows (the ghost fluid method). *J Comput Phys* 1999;125:457–92.
- [8] Kadioglu SY, Sussman M. Adaptive solution techniques for simulating underwater explosions and implosions. *J Comput Phys* 2008;227:2083–104.
- [9] Matula TJ, Hilmo PR, Storey BD, Szeri AJ. Radial response of individual bubbles subjected to shock wave lithotripsy pulses in vitro. *Phys Fluids* 2002;14:913–21.
- [10] Wardlaw A. Underwater explosion test cases. Technical report IHTR 2069 ADB238684, Office of Naval Research, 1998.
- [11] Müller S, Bachmann M, Kröninger D, Kurz T, Helluy P. Comparison and validation of compressible ow simulations of laser-induced cavitation bubbles. *Comput Fluids* 2009;38:1850–62.
- [12] Marek R, Straub J. Analysis of the evaporation coefficient and the condensation coefficient of water. *Int J Heat Mass Transfer* 2001;44:39–53.
- [13] Hao Y, Prosperetti A. The dynamics of vapor bubbles in acoustic pressure fields. *Phys Fluids* 1999;11:2008–19.
- [14] Puente GF, Bonetto FJ. Proposed method to estimate the liquid–vapor accommodation coefficient based on experimental sonoluminescence data. *Phys Rev E* 2005;71:056309.
- [15] Fuster D, Hauke G, Dopazo C. Influence of the accommodation coefficient on nonlinear bubble oscillations. *J Acoust Soc Am* 2010;128:5–10.
- [16] Tomita Y, Shima A. Mechanisms of impulsive pressure generation and damage pit formation by bubble collapse. *J Fluid Mech* 1986;169:535–64.
- [17] Vogel A, Lauterborn W, Timm R. Optical and acoustic investigations of the dynamics of laser-produced cavitation bubbles near a solid boundary. *J Fluid Mech* 1989;206:299–338.
- [18] Philipp A, Lauterborn W. Cavitation erosion by single laser-produced bubbles. *J Fluid Mech* 1998;361:75–116.
- [19] Bremond N, Arora M, Dammer SM, Lohse D. 2006 Interaction of cavitation bubbles on a wall. *Phys Fluids* 2006;18:121505.
- [20] Gonzalez-Avila SR, Klaseboer E, Khoo BC, Ohl CD. Cavitation bubble dynamics in a liquid gap of variable height. *J Fluid Mech* 2011;682:241–60.
- [21] Tong RP, Schiffrs WP, Shaw SJ, Blake JR, Emmony DC. The role of ‘splashing’ in the collapse of a laser-generated cavity near a rigid boundary. *J Fluid Mech* 1999;380:339–61.
- [22] Silberrad D. Propeller erosion. *Engineering* 1912:33–5.
- [23] Matula TJ, Hilmo PR, Bailey MR, Crum LA. In vitro sololuminescence and sonochemistry studies with an electrohydraulic shock-wave lithotripter. *Ultrasound Med Biol* 2002;28(9):1199–207.
- [24] Illoreta JL, Fung NM, Szeri AJ. Dynamics of bubbles near a rigid surface subjected to a lithotripter shock wave. Part 1. Consequences of interference between incident and reflected waves. *J Fluid Mech* 2008;616:43–61.
- [25] Jamaluddin AR, Ball GJ, Turangan CK, Leighton TG. The collapse of single bubbles and approximation of the far-field acoustic emission for cavitation induced by shock wave lithotripsy. *J Fluid Mech* 2011;677:305–41.
- [26] Bohner M, Fischer R, Gscheidle R. *Fachkunde Kraftfahrzeugtechnik*. Haan-Gruiten: Verlag Europa-Lehrmittel; 2001 [in German].
- [27] Plesset MS, Chapman RB. Collapse of an initially spherical vapour cavity in the neighbourhood of a solid wall. *J Fluid Mech* 1971;47:283–90.
- [28] Zhang S, Duncan JH, Chahine GL. The final stage of the collapse of a cavitation bubble near a rigid wall. *J Fluid Mech* 1993;257:147–81.
- [29] Blake JR, Pearson A, Otto SR. Boundary integral methods for cavitation bubbles near boundaries. In: *Proc fourth international symposium on cavitation*. CA (USA): California Institute of Technology; 2001.
- [30] Popinet S, Zaleski S. Bubble collapse near a solid boundary: a numerical study of the influence of viscosity. *J Fluid Mech* 2002;464:137–63.
- [31] Sussman M. A second order coupled level set and volume-of-fluid method for computing growth and collapse of a vapor bubble. *J Comput Phys* 2003;187:110–36.
- [32] Müller S, Helluy P, Ballmann J. Numerical simulation of a single bubble by compressible two-phase fluids. *Int J Numer Meth Fluids* 2010;62:591–631.
- [33] Saurel R, Abgrall R. A simple method for compressible multifluid flows. *SIAM J Sci Comput* 1999;21(3):1115–45.
- [34] Klaseboer E, Turangan CK, Khoo BC. Dynamic behaviour of a bubble near an elastic infinite interface. *Int J Multiphase Flow* 2006;32:1110–22.
- [35] Freund JB, Shukla RK, Evan AP. Shock-induced bubble jetting into a viscous fluid with application to tissue injury in shock-wave lithotripsy. *J Acoust Soc Am* 2009;126(5):2746–56.
- [36] Shukla RK, Pantano C, Freund JB. An interface capturing method for the simulation of multi-phase compressible flows. *J Comput Phys* 2010;229:7411–39.
- [37] Shima A, Nakajima K. The collapse of a non-hemispherical bubble attached to a solid wall. *J Fluid Mech* 1977;80:369–91.
- [38] Blake JR, Robinson PB, Shima A, Tomita Y. Interaction of two cavitation bubbles with a rigid boundary. *J Fluid Mech* 1993;255:707–21.
- [39] Pearson A, Blake JR, Otto SR. Jets in bubbles. *J Eng Math* 2004;48:391–412.
- [40] Calvisi ML, Illoreta JL, Szeri AJ. Dynamics of bubbles near a rigid surface subjected to a lithotripter shock wave. Part 2. Reflected shock intensifies non-spherical cavitation collapse. *J Fluid Mech* 2008;616:63–97.
- [41] Johnsen E, Colonius T. Shock-induced collapse of a gas bubble in shockwave lithotripsy. *J Acoust Soc Am* 2008;124(4):2011–20.
- [42] Lorenzen WE, Cline HE. Marching cubes a high resolution 3D surface construction algorithm. *Comput Graph* 1987;21(4):163–9.
- [43] Jiang GS, Shu CW. Efficient implementation of weighted ENO schemes. *J Comput Phys* 1996;126:202–28.
- [44] Shu CW, Osher S. Efficient implementation of essentially non-oscillatory shock capturing schemes. *J Comput Phys* 1988;77:439–71.
- [45] Toro EF. *Riemann solvers and numerical methods for fluid dynamics: a practical introduction*. Springer; 1997.
- [46] Hu XY, Khoo BC. An interface interaction method for compressible multifluids. *J Comput Phys* 2004;198:35–64.
- [47] Fujikawa S, Akamatsu T. Effects of the non-equilibrium condensation of vapour on the pressure wave produced by the collapse of a bubble in a liquid. *J Fluid Mech* 1980;97:481–512.
- [48] Schrage RW. *A theoretical study of interphase mass transfer*. Columbia University Press; 1953.
- [49] Brennen CE. *Cavitation and bubble dynamics*. Oxford University Press; 1995.
- [50] Hu XY, Adams NA, Johnsen E, Iaccarino G. Modeling full-Mach-range cavitating flow with sharp interface model. In: *Proceedings of the 2008 summer program CTR*, Stanford, CA, 2008.
- [51] Young FR. *Cavitation*. Imperial College Press; 1999.
- [52] Sezal IH. *compressible dynamics of cavitating 3-D multi-phase flows*. PhD thesis, Technische Universität München, Verlag Dr. Hut; 2009.
- [53] Niederhaus JHJ, Greenough JA, Oakley JG, Ranjan D, Anderson MH, Bonazza R. A computational parameter study for the three-dimensional shock-bubble interaction. *J Fluid Mech* 2008;594:85–124.
- [54] Hung CF, Hwangfu JJ. Experimental study of the behaviour of mini-charge underwater explosion bubbles near different boundaries. *J Fluid Mech* 2010;651:55–80.
- [55] Ohl CD, Philipp A, Lauterborn W. Cavitation bubble collapse studied at 20 million frames per second. *Ann Phys* 1995;507:26–34.
- [56] Akhatov I, Lindau O, Topolnikov A, Mettin R, Vakhitova N, Lauterborn W. Collapse and rebound of a laser-induced cavitation bubble. *Phys Fluids* 2001;13:2805–19.
- [57] Shaw SJ, Spelt PDM. Shock emission from collapsing gas bubbles. *J Fluid Mech* 2010;646:363–73.
- [58] Dabiri S, Sirignano WA, Joseph DD. Interaction between a cavitation bubble and shear flow. *J Fluid Mech* 2010;651:93–116.